

A general model for the CO–H₂ conversion factor in galaxies with applications to the star formation law

Desika Narayanan,^{1*}† Mark R. Krumholz,² Eve C. Ostriker³ and Lars Hernquist⁴

¹Steward Observatory, University of Arizona, 933 N Cherry Ave, Tucson, AZ 85721, USA

²Department of Astronomy and Astrophysics, University of California, Santa Cruz, CA 95064, USA

³Department of Astronomy, University of Maryland, College Park, MD 20742, USA

⁴Harvard–Smithsonian Center for Astrophysics, 60 Garden Street, Cambridge, MA 02138, USA

Accepted 2012 January 11. Received 2012 January 10; in original form 2011 October 17

ABSTRACT

The most common means of converting an observed CO line intensity into a molecular gas mass requires the use of a conversion factor (X_{CO}). While in the Milky Way this quantity does not appear to vary significantly, there is good reason to believe that X_{CO} will depend on the larger-scale galactic environment. With sensitive instruments pushing detections to increasingly high redshift, characterizing X_{CO} as a function of physical conditions is crucial to our understanding of galaxy evolution. Utilizing numerical models, we investigate how varying metallicities, gas temperatures and velocity dispersions in galaxies impacts the way CO line emission traces the underlying H₂ gas mass, and under what circumstances X_{CO} may differ from the Galactic mean value. We find that, due to the combined effects of increased gas temperature and velocity dispersion, X_{CO} is depressed below the Galactic mean in high surface density environments such as ultraluminous infrared galaxies (ULIRGs). In contrast, in low-metallicity environments, X_{CO} tends to be higher than in the Milky Way, due to photodissociation of CO in metal-poor clouds. At higher redshifts, gas-rich discs may have gravitationally unstable clumps that are warm (due to increased star formation) and have elevated velocity dispersions. These discs tend to have X_{CO} values ranging between present-epoch gas-rich mergers and quiescent discs at low z . This model shows that *on average* mergers do have lower X_{CO} values than disc galaxies, though there is significant overlap. X_{CO} varies smoothly with the local conditions within a galaxy, and is not a function of global galaxy morphology. We combine our results to provide a general fitting formula for X_{CO} as a function of CO line intensity and metallicity. We show that replacing the traditional approach of using one constant X_{CO} for starbursts and another for discs with our best-fitting function produces star formation laws that are continuous rather than bimodal, and that have significantly reduced scatter.

Key words: ISM: clouds – ISM: molecules – galaxies: interactions – galaxies: ISM – galaxies: starburst – galaxies: star formation.

1 INTRODUCTION

As the building block of stars, H₂ is arguably the most important molecule in astrophysics. Ironically, however, it is also one of the more observationally elusive. With no permanent dipole moment, H₂ is best directly detected via its first quadrupole line. This line lies at ~ 500 K above ground, significantly above the ~ 10 K typical of the cold molecular interstellar medium (ISM), and in a spectral region with relatively low atmospheric transmission. As a result, giant molecular clouds (GMCs) are often studied via tracer molecules.

The ground-state rotational transition of carbon monoxide [¹²CO ($J = 1-0$), hereafter CO] is one of the most common tracers of H₂ in GMCs owing to its relatively high abundance ($\sim 10^{-4}$ /H₂ in the Galaxy; Lee, Bettens & Herbst 1996), the high atmospheric transmission at ~ 3 mm where the $J = 1-0$ line lies, and the low temperatures and densities required for CO excitation (~ 5 K, $\sim 10^2$ – 10^3 cm⁻³). However, using CO to trace H₂ does not come without uncertainty. At the basis of the interpretation of CO observations is the conversion between CO spectral line intensity and H₂ gas mass, the so-called CO–H₂ conversion factor.

The CO–H₂ conversion factor is defined as

$$X_{\text{CO}} = \frac{N_{\text{H}_2}}{W_{\text{CO}}} \quad (1)$$

*E-mail: dnarayanan@as.arizona.edu

†Bart J. Bok Fellow.

where N_{H_2} is the molecular gas column density, and W_{CO} is the velocity-integrated CO line intensity (measured in K-km s^{-1}). Alternatively, the conversion factor can be defined as the ratio of the molecular gas mass and CO line luminosity:

$$\alpha_{\text{CO}} = \frac{M_{\text{gas}}}{L_{\text{CO}}}. \quad (2)$$

X_{CO} and α_{CO} are easily related via

$$\begin{aligned} X_{\text{CO}} (\text{cm}^{-2}(\text{K} - \text{kms}^{-1})^{-1}) \\ = 6.3 \times 10^{19} \times \alpha_{\text{CO}} (\text{M}_{\odot} \text{pc}^{-2}(\text{K} - \text{kms}^{-1})^{-1}). \end{aligned} \quad (3)$$

Hereafter, we refer to the CO–H₂ conversion factor in terms of X_{CO} ,¹ though plot in terms of both X_{CO} and α_{CO} .

Despite potential variations in CO abundances, radiative transfer effects and varying H₂ gas fractions, a variety of independent measurements of H₂ gas mass in GMCs have shown that the CO–H₂ conversion factor in Galactic clouds is reasonably constant, with $X_{\text{CO}} \approx 2\text{--}4 \times 10^{20} \text{ cm}^{-2}/\text{K-km s}^{-1}$ [$\alpha_{\text{CO}} \approx 3\text{--}6 \text{ M}_{\odot} \text{pc}^{-2}(\text{K} - \text{kms}^{-1})^{-1}$]. Methods for obtaining independent measurements of H₂ gas mass include (i) assuming the GMCs are in virial equilibrium, and utilizing the CO line width to derive the H₂ mass within the CO emitting region (e.g. Larson 1981; Solomon et al. 1987); (ii) inferred dust masses and an assumed dust-to-gas mass ratio (Dickman 1975; de Vries, Thaddeus & Heithausen 1987; Guelin et al. 1993; Dame, Hartmann & Thaddeus 2001; Lombardi, Alves & Lada 2006; Draine & Li 2007; Pineda, Caselli & Goodman 2008; Leroy et al. 2011; Magdis et al. 2011) and (iii) γ -ray emission arising from the interaction of cosmic rays with H₂ (Bloemen et al. 1986; Bertsch et al. 1993; Strong & Mattox 1996; Hunter et al. 1997; Abdo et al. 2010b; Delahaye et al. 2011). Beyond this, observations of GMCs in the Local Group suggest that a similar CO–H₂ conversion factor may apply for some clouds outside of our own Galaxy (Rosolowsky et al. 2003; Blitz et al. 2007; Donovan Meyer et al. 2012). Numerical models of molecular clouds on both resolved and galaxy-wide scales have indicated that a relatively constant CO–H₂ conversion factor in the Galaxy and nearby galaxies may naturally arise from GMCs that have a limited range in surface densities, metallicities and velocity dispersions (Glover & Mac Low 2011; Feldmann, Gnedin & Kravtsov 2011; Narayanan et al. 2011b; Shetty et al. 2011a).

In recent years, a number of observational studies have provided evidence for at least two physical regimes where the CO–H₂ conversion factor departs from the ‘standard’ Milky Way value. The first is in high-surface density environments. Interferometric observations of present-epoch galaxy mergers by Scoville et al. (1991), Downes, Solomon & Radford (1993), Solomon et al. (1997), Downes & Solomon (2003), Hinz & Rieke (2006), Meier et al. (2010) and Downes & Solomon (1998) showed that using a Milky Way X_{CO} would cause the inferred H₂ gas mass to exceed the dynamical mass of the CO-emitting region for some galaxies. This implies that the CO–H₂ conversion factor should be lower than the Galactic mean in high-surface density environments. More recent observations of $z \sim 2$ submillimetre galaxies (SMGs) by Tacconi et al. (2008) suggested a similar result for high-redshift starbursts. Similarly, observations of GMCs towards the Galactic Centre indicate that X_{CO} may be lower in this high-surface density environment (Oka et al. 1998).

Secondly, in low-metallicity environments at both low and high z , the CO–H₂ conversion factor may be larger than the Milky Way mean value (Wilson 1995; Arimoto, Sofue & Tsujimoto 1996; Israel

1997; Boselli, Lequeux & Gavazzi 2002; Leroy et al. 2006; Bolatto et al. 2008; Leroy et al. 2011; Genzel et al. 2012), though there is some debate over this (see summaries in Blitz et al. 2007, and the Appendix of Tacconi et al. 2008). Observations have suggested that the X -factor may scale as $X \propto (\text{O}/\text{H})^{-b}$ where $b = 1\text{--}2.7$ (Arimoto et al. 1996; Israel 1997).

The fact that these two effects drive X_{CO} in opposite directions complicates the interpretation of CO detections from high-redshift systems where galaxies display a large range in metallicities (e.g. Shapley et al. 2004; Shapley 2011; Genzel et al. 2012) and gas surface densities (e.g. Bothwell et al. 2010; Daddi et al. 2010a; Genzel et al. 2010; Narayanan et al. 2011a). Further muddying the interpretation of high- z molecular line emission is the fact that there are not always clear analogues of high-redshift galaxies in the present-day Universe. For example, relatively unperturbed discs at $z \sim 2$ oftentimes have surface densities, star formation rates (SFR) and velocity dispersions comparable to local galaxy mergers (Daddi et al. 2005, 2010a; Krumholz & Dekel 2010; Genzel et al. 2011), though (sometimes) lower metallicities (Cresci et al. 2010). Similarly, even the most heavily star-forming galaxies at $z \sim 2$, SMGs, at times show dynamically cold molecular discs even when they are potentially the result of mergers (Narayanan et al. 2009, 2010a; Carilli et al. 2010; Engel et al. 2010). Converting CO line intensity to H₂ gas masses is a multi-faceted problem that involves understanding how galactic environment sets the X -factor.

Over the last two decades, models of GMC evolution have made substantive headway in elucidating the variation of X_{CO} with physical properties of molecular clouds. The earliest GMC models utilized 1D radiative transfer with spherical cloud models (e.g. Kutner & Leung 1985; Wall 2007). Photodissociation region (PDR) models furthered these studies by including the formation and destruction pathways of CO (Bell et al. 2006; Bell, Viti & Williams 2007; Meijerink, Spaans & Israel 2007). More recently, magnetohydrodynamic models of GMC evolution with time-dependent chemistry by Glover et al. (2010) and Glover & Mac Low (2011) coupled with radiative transfer calculations (Shetty et al. 2011a,b) have investigated X_{CO} on the scales of individual GMCs, and its dependence on the physical environment.

Compared to models of isolated GMCs, there are relatively few simulations exploring the effect of the larger galactic environment on the X -factor. Maloney & Black (1988) presented some of the earliest models which explored the effects of changing individual physical parameters in isolation on the CO–H₂ conversion factor. Very recently, Feldmann et al. (2011) have tied the GMC models of Glover & Mac Low (2011) to cosmological simulations of galaxy evolution to investigate X_{CO} on galaxy-wide scales in relatively quiescent disc galaxies. Building on these models, as well as what has been learned in the studies of Glover & Mac Low (2011), Shetty et al. (2011a) and Wolfire, Hollenbach & McKee (2010), in Narayanan et al. (2011b), we combined dust and molecular line radiative transfer calculations with hydrodynamic simulations of galaxies in evolution in order to develop a model that aims to capture the CO line emission from GMCs on galaxy-wide scales.

In this paper, utilizing the methodology we developed in Narayanan et al. (2011b), we investigate the effect of galactic environment in setting the CO–H₂ conversion factor in galaxies at low and high redshifts. Our paper is organized as follows. In Section 2, we summarize the methodology developed in Narayanan et al. (2011b) and employed here. We note that while Section 2 is a shorter summary, a more complete description is presented in Appendix A. In Section 3, we investigate the role of galactic environment on X_{CO} , focusing on isolated disc galaxies (Section 3.1),

¹ In the literature, X_{CO} is sometimes referred to as the X -factor, and we shall use the two interchangeably.

galaxies at low metallicity (Section 3.2), high-surface density (Section 3.3) and high redshift (Section 3.4). Building on these results, in Section 4, we develop a functional form for calculating X_{CO} from observations of galaxies and, as an application, utilize these to interpret Kennicutt–Schmidt (KS) SFR relations at low and high redshift. In Section 5, we discuss our results in the context of other theoretical models, and in Section 6, we summarize our main results.

2 SUMMARY OF SIMULATION METHODOLOGY

Our main goal is to simulate the impact of galactic environment on the H_2 content and CO emission from galaxies. This involves simulating the evolution of galaxies, the physical state of the molecular ISM, and the radiative transfer of CO lines through GMCs and through galaxies. Because much of the methodology has been described in a previous paper by us (Narayanan et al. 2011b), we briefly summarize our approach here, and defer the quantitative details to the Appendix.

We first require model galaxies to analyse. We simulate the hydrodynamic evolution of disc galaxies in isolation and galaxy mergers over a range of galaxy masses, merger mass ratios and redshifts utilizing a modified version of the publicly available code, GADGET-2. These simulations provide information regarding the kinematic structure, mass and metal distribution of the ISM, as well as the stellar populations. Table A1 summarizes the model properties.

The remainder of our calculations occur in post-processing. We smooth the smoothed particle hydrodynamic (SPH) results on to an adaptive mesh. We require knowledge of the physical and chemical state of the molecular clouds in our model galaxies. We assume the cold H_2 gas is bound in spherical GMCs with H_2 fractions calculated following the models of Krumholz, McKee & Tumlinson (2008) and Krumholz, McKee & Tumlinson (2009a). Carbon is assumed to have a uniform abundance within these clouds of $1.5 \times 10^{-4} \times Z'$, where Z' is the metallicity with respect to solar. The fraction of carbon locked up in CO is determined following the models of Wolfire et al. (2010), and have an explicit dependence on the metallicity. GMCs that have a surface density greater than $100 M_{\odot} \text{pc}^{-2}$ are considered resolved. GMCs that are not resolved (typically low-mass GMCs in large cells in the adaptive mesh) have a floor surface density of the aforementioned value imposed, consistent with observations of Local Group GMCs (e.g. Bolatto et al. 2008; Fukui & Kawamura 2010). Unresolved GMCs have velocity dispersions equal to the virial velocity of the GMC, whereas resolved GMCs have velocity dispersions determined directly from the simulations.

The temperature of the GMCs is determined via a balance of the various heating processes on the gas (here, photoelectric effect, cosmic rays and energy exchange with dust), and line cooling. The dust temperature is calculated via the publicly available dust radiative transfer code, SUNRISE (Jonsson, Groves & Cox 2010). The cosmic ray heating rate is assumed to take on the mean Galactic value (except as described in Appendix C). Utilizing this model, the temperature ranges typically from ~ 10 K in quiescent GMCs to > 100 K in the centres of starbursts (Narayanan et al. 2011b).

Once the physical and chemical state of the ISM is known, we are prepared to model the CO line emission via radiative transfer calculations. The emergent CO line emission from the GMCs is calculated via an escape probability formalism (Krumholz & Thompson 2007). This radiation is then followed through the galaxy in order to account for radiative transfer processes on galaxy-wide

scales (Narayanan et al. 2006, 2011b). With these calculations, we know the thermal and chemical state of the molecular ISM in our model galaxies, the synthetic broad-band SEDs and the modelled CO emission line spectra. At this point, we are in a position to understand variations in the CO– H_2 conversion factor. We remind the reader that further details regarding the implementation of these models can be found in the Appendix.

We note that in order to alleviate confusion between simulation points and observational data on plots, we will employ a system throughout this work in which filled symbols exclusively refer to observational data, and open symbols refer to simulation results.

3 THE EFFECT OF GALACTIC ENVIRONMENT ON X_{CO}

Our general goal is to understand how X_{CO} depends on the physical environment in galaxies, and how it may vary with observable properties of galaxies. In order to do this, we must first develop intuition as to how various physical parameters affect X_{CO} . In this section, we examine how X_{CO} varies from the Galactic mean in low-metallicity environments, high-surface density environments and at high redshift.

Quantitatively, we define the mean X_{CO} from a galaxy as:

$$\langle X_{\text{CO}} \rangle = \frac{\int \Sigma_{\text{H}_2} dA}{\int W_{\text{CO}} dA} \quad (4)$$

which is equivalent to a luminosity-weighted X_{CO} over all GMCs in the galaxy.

3.1 Review of X_{CO} in $z = 0$ quiescent disc galaxies

We begin by considering X_{CO} in disc galaxies at $z = 0$ with metallicities around solar ($Z' \approx 1$). These galaxies have mean X -factors comparable to the Galactic mean and will serve as the ‘control’ sample from which we will discuss variations in physical parameters.

Recalling Section 2, and referring to the Appendix, when clouds are not resolved, we impose a floor surface density of $100 M_{\odot} \text{pc}^{-2}$. In these GMCs, the velocity dispersion is the virial velocity of the cloud. In our model $z = 0$ disc galaxies, gas compressions within the galaxy are unable to cause significant deviations from these subresolution values of $N_{\text{H}_2} \sim 10^{22} \text{cm}^{-2}$ and $\sigma \sim 1 - 5 \text{ km s}^{-1}$. In this regime, the temperatures of the GMCs typically fall to $\sim 8 - 10$ K. This is the usual temperature where cosmic rays dominate gas heating in our model; the densities are not sufficiently high for any of the heating processes to increase the gas temperatures drastically. At \sim solar metallicities, a sufficient column of dust can easily build up to protect the CO from photodissociation, and most of the carbon in molecular clouds is in the form of CO. With these modest conditions in the clouds, and little variation throughout the galaxy (see fig. 2 of Narayanan et al. 2011b), the modelled X_{CO} tends to be \sim a few $\times 10^{20} \text{ cm}^{-2} \text{K-km s}^{-1}$ (i.e. similar to the Milky Way mean), with the only notable exception being GMCs towards the galactic centre (Narayanan et al. 2011b).

As pointed out by Narayanan et al. (2011b), while various sub-resolution techniques are folded into our model disc galaxies, that we see relatively little variation in the GMC properties in our model $z = 0$ discs is a statement that the galactic environment is not extreme enough to cause significant deviations from the default surface densities and velocity dispersions. The temperatures and velocity dispersions are allowed to vary freely with galactic environment, and the surface densities have a floor value similar to

actual GMCs (Blitz et al. 2007; Bolatto et al. 2008). As shown by Shetty et al. (2011a), GMCs with physical parameters comparable to those observed in Galactic GMCs exhibit X_{CO} values close to the Galactic mean, $X_{\text{CO}} \approx 2\text{--}4 \times 10^{20} \text{cm}^{-2}/\text{K-kms}^{-1}$ [$\alpha_{\text{CO}} \approx 3\text{--}6 \text{M}_{\odot} \text{pc}^{-2}(\text{K} - \text{kms}^{-1})^{-1}$]. As we will show, in the present Universe, low-metallicity galaxies and, in some cases, high-redshift discs, the physical properties of GMCs vary sufficiently that this is no longer the case.

3.2 The effects of metallicity on X_{CO}

The metallicity of the gas can have a strong effect on the CO–H₂ conversion factor. In metal-poor gas, it is possible to have ‘CO-dark’ molecular clouds (Papadopoulos, Thi & Viti 2002; Wolfire et al. 2010). In these regions, H₂ can self-shield to protect itself from photodissociating UV radiation, whereas CO cannot and requires dust to survive (Sternberg & Dalgarno 1995; Hollenbach & Tielens 1999). In these cases, we expect a larger fraction of CO-dark clouds and a rise in the CO–H₂ conversion factor (Maloney & Black 1988; Wolfire et al. 2010; Shetty et al. 2011b; Feldmann et al. 2011).

In Fig. 1, we plot the emission-weighted mean X_{CO} for our model $z = 0$ isolated disc galaxies as a function of metallicity with filled contours. To control for surface density effects, we plot models with $\Sigma_{\text{H}_2} \approx 100 \text{M}_{\odot} \text{pc}^{-2}$. The contours indicate the number of snapshots in a given $X_{\text{CO}}\text{--}Z'$ bin. The outer dashed contour denotes the contour that encompasses all of our models, at any gas surface density.

The lowest metallicity model galaxies all have relatively high mean X -factors compared to the \sim solar metallicity galaxies. The lowest metallicity models can have mean X -factors approximately an order of magnitude greater than the Galactic mean. As the galaxies evolve and the ISM becomes enriched with metals, the carbon is almost exclusively in the form of CO, and the X -factor decreases.

The predicted $X_{\text{CO}}\text{--}Z'$ relation in Fig. 1 matches well with recent observational data. Overlaid, we plot recent results from resolved regions in nearby galaxies from Bolatto et al. (2008), Leroy et al. (2011) and Genzel et al. (2012). Note that Σ_{H_2} (and thus X_{CO}) in the observations depends on an estimate of the gas mass, which is

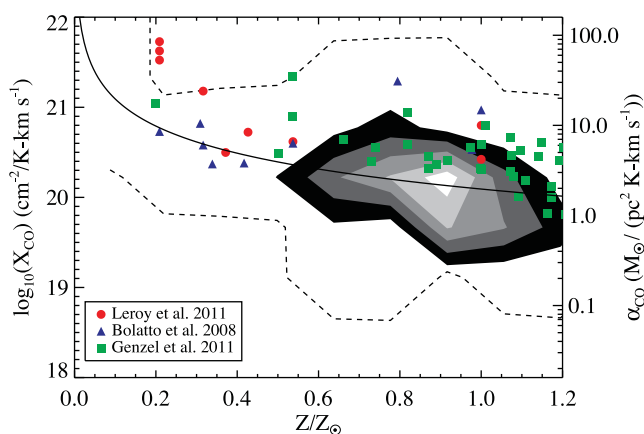


Figure 1. X_{CO} versus mass-weighted mean metallicity (in units of solar) for all $z = 0$ model galaxies with $\Sigma_{\text{H}_2} \sim 100 \text{M}_{\odot} \text{pc}^{-2}$. The contours represent the number of snapshots in a given $X_{\text{CO}}\text{--}Z'$ bin, with the numbers increasing with increasing lightness of the contour. The dashed line outer contour encompasses all model galaxies, regardless of their gas surface density. Overlaid are observational data points from Bolatto et al. (2008), Leroy et al. (2011) and Genzel et al. (2012). The solid line shows our best fit to the simulations and is expressed in equation (8) and described in Section 4.

obtained with various methods for these studies.² Both the observations and models show an upward trend in X_{CO} with decreasing metallicity. While we defer a discussion of fitting X_{CO} in terms of Z' to Section 4, we denote our best-fitting model (discussed in equation 8) by the solid line in Fig. 1.

We should note that the contours in Fig. 1 indicate the range of possible X -factors at a given metallicity as returned by our models. They are not cosmological, and so do not connote any particular probabilities. The simple fact that observed data points lie within the contours with a similar $X_{\text{CO}}\text{--}Z'$ trend suggests a reasonable match between our models and observed galaxies. When examining the outer contour that encompasses all of our models (and not just those at a given surface density as in the grey-scale contours), it is clear that there is a significant dispersion in X_{CO} on either side of the best-fitting line in Fig. 1. Moreover, there is a significant dispersion in the observed data at a given metallicity (especially noticeable near $Z' \approx 1$). This suggests that there is a second parameter controlling the X -factor in galaxies, aside from metallicity. As we will show in the next section, this is the dynamical and thermal state of the molecular ISM.

3.3 High surface density galaxies

3.3.1 Large temperatures and velocity dispersions

On average, in regions of high surface density, the emission-weighted mean X_{CO} in a galaxy is lower than the Galactic mean value of $\sim 2\text{--}4 \times 10^{20} \text{cm}^{-2}/\text{K-km s}^{-1}$. This has been shown observationally by Tacconi et al. (2008), and seen in the models of Narayanan et al. (2011b).

By itself, an increase in surface density does not cause X_{CO} to decrease. Rather, the opposite is true: per equation (1), at high surface densities, X_{CO} would *increase* if W_{CO} were fixed. However, in high- Σ_{H_2} regions, the velocity-integrated line intensity, W_{CO} , in fact increases even more rapidly than Σ_{H_2} , causing a net decrease in X_{CO} . To see why this is the case, consider the physical processes that are typically associated with increased surface densities.

First, regions of high surface density are associated with higher SFRs (Kennicutt 1998a; Krumholz, McKee & Tumlinson 2009b; Ostriker, McKee & Leroy 2010; Ostriker & Shetty 2011). While a variety of theories exist as to why this is the case (see a review of some of these models in Tan 2010), in our simulations this is due to the fact that we explicitly tie our SFRs to the volumetric gas density on small scales. With high SFRs come hotter dust temperatures as the UV radiation heats the nearby dust grains. When the gas densities are $\gtrsim 10^4 \text{cm}^{-3}$, the dust and gas exchange energy efficiently, and the gas temperature approaches the dust temperature (Goldsmith 2001; Juvela & Ysard 2011). Hence, in regions of high surface density, the increased dust temperature driven by the higher SFRs causes an increase in the gas kinetic temperature. Because the CO ($J = 1\text{--}0$) line is thermalized at relatively low densities, the brightness temperature of the line is comparable to the kinetic temperature of the gas, and is thus increased in regions of

² Bolatto et al. (2008) assume clouds are virialized; if instead clouds are marginally bound, then X_{CO} would decrease. Leroy et al. (2011) use infrared emission to derive dust masses, and H I observations to derive a dust-to-gas ratio. If this dust-to-gas ratio does not map to the H₂ gas, the derived X_{CO} will change accordingly. Genzel et al. (2010) assume a scaling relation $\Sigma_{\text{SFR}} \propto \Sigma_{\text{gas}}^{1.1}$. If a steeper relation were adopted (cf. Section 4.2), then the values of X_{CO} corresponding to high values of Σ_{SFR} would decrease somewhat.

high surface density. For low-redshift galaxies, the easiest way to increase the surface density tends to be through merging activity and the associated tidal torques which drive gaseous inflows into the nuclear region (Barnes & Hernquist 1991, 1996; Mihos & Hernquist 1994b, 1996), though higher-redshift discs can have relatively large surface densities simply due to gravitational instabilities in extremely gas-rich clumps (Springel, Di Matteo & Hernquist 2005; Bournaud et al. 2010).

Secondly, in the simulations, high surface densities in gas are typically accompanied by high velocity dispersions. This generally means some level of merging activity in low-redshift galaxies, and either merging activity or unstable gas clumps in high-redshift discs. In major mergers, the emission-weighted velocity dispersions can be as high as $\sim 50\text{--}100 \text{ km s}^{-1}$.

The increased velocity dispersion and kinetic temperature contribute roughly equally to increasing the velocity-integrated line intensity. During a merger, the temperature and velocity dispersion individually increase enough to offset the increase in the gas surface density, and in combination tend to drive the emission-weighted mean X_{CO} for a galaxy below the Milky Way average. In regions of high surface density, the emission-weighted mean X_{CO} tends to decrease on average. In Section 3.4, we detail specific numbers for a sample merger that serves as an example for this effect.

We can see this more explicitly in Fig. 2, where we plot the mean X_{CO} versus mean surface density for the starburst snapshots in our low-redshift sample of galaxies. The starburst snapshots are defined as the snapshots where the SFR peaks for a given model and are categorized by the merger mass ratio (1:1, 1:3 and 1:10). The mean surface density is defined as the mass-weighted surface density over all GMCs, i , in the galaxy:

$$\langle \Sigma_{\text{H}_2} \rangle = \frac{\sum_i \Sigma_{\text{H}_2,i} \times M_{\text{H}_2,i}}{\sum_i M_{\text{H}_2,i}} \quad (5)$$

Henceforth, when we refer to the surface density of the galaxy, we refer to the mean surface density defined by equation (5). We note that this is different from the commonly used definition $\Sigma_{\text{H}_2} = M_{\text{H}_2}/A$, where A is the area within an observational aperture. We refrain from the latter definition as it is dependent on the choice of

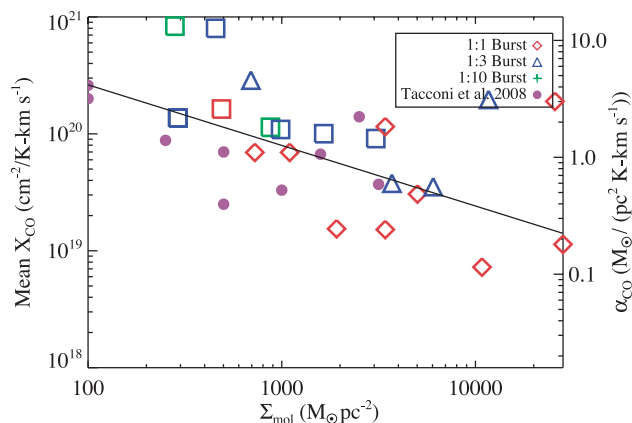


Figure 2. Mean X_{CO} versus mass-weighted mean surface density for $z=0$ model mergers when they are undergoing a starburst (e.g. the snapshots with the peak SFRs). The plotting symbols are shown in the legend, though a given symbol may be replaced by a square if the metallicity is lower than $0.5 Z_{\odot}$. The purple filled circles represent the compiled data from Tacconi et al. (2008). The black solid line is the best fit for all simulation snapshots from equation (10), and is discussed in Section 4.

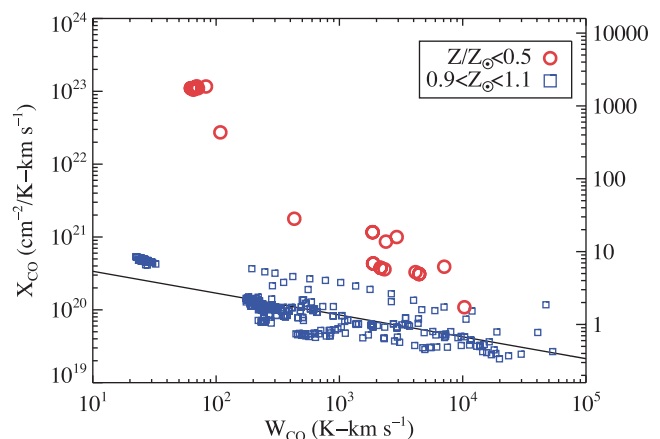


Figure 3. X_{CO} versus CO line intensity, W_{CO} for $z=0$ 1:1 galaxy mergers in two distinct metallicity bins. In this case, W_{CO} is a surrogate for Σ_{H_2} that is an actual observable (and relatable via X_{CO}). At a given metallicity, X_{CO} decreases with CO intensity due to the larger number of CO-dark GMCs in these galaxies. The solid line shows the best-fitting model (cf. Section 4) for a metallicity of $Z' = 1$.

scale. (Σ_{H_2}) can be thought of as the surface density at which most of the mass resides. Immediately, we see two trends in Fig. 2.

First, with increasing surface density, we see decreasing mean X_{CO} due to the warm and high velocity dispersion gas associated with merging systems. Secondly, the most violent mergers tend to have the lowest mean X_{CO} values, whereas lower mass ratio mergers (1:3) have less extreme conditions, and thus X -factors more comparable to the Galactic mean value. The purple circles in Fig. 2 note observational points from Tacconi et al. (2008); the models and data show broad agreement.³

The open squares in Fig. 2 are points from our models with mean metallicities less than $Z' < 0.5$. Careful examination of these points shows that some of them have rather large X -factors. As we discussed in Section 3.2, lower metallicity galaxies have larger mass fractions of CO-dark clouds, and thus higher X -factors.

In Fig. 3, we demonstrate more explicitly the effect of metallicity on the X_{CO} –surface density relationship. Because we find it useful in a forthcoming section (Section 4) to parametrize X_{CO} in terms of the observable velocity-integrated CO intensity, W_{CO} as an observable, rather than Σ_{H_2} , we plot X_{CO} against W_{CO} in Fig. 3. W_{CO} is defined as the luminosity-weighted line intensity from all GMCs in the galaxy. We plot the X_{CO} – W_{CO} relationship for all snapshots of all 1:1 $z = 0$ major mergers within two distinct metallicity ranges. The selected metallicity ranges are arbitrary, and are chosen simply to highlight the influence of metallicity. As is clear, the lowest metallicity points in Fig. 3 have the highest X -factors, and the reverse is true for the highest metallicity points. For each metallicity bin, the trend is such that increasing W_{CO} (or Σ_{H_2}) correlates with decreasing X_{CO} , though the normalization varies with metallicity. This informs our fitting formula in Section 4.

Returning to Fig. 2, we make a final point that there is a large dispersion in X_{CO} for the merger models. Both the 1:3 models and 1:1

³ We caution that our definition of (Σ_{H_2}) is a mass-weighted surface density, and is different from the surface density defined by the Tacconi et al. data, M_{H_2}/A . In the limit of a large volume filling factor, these values will approach one another. The observed data closer to $\Sigma_{\text{mol}} = 100 M_{\odot} \text{ pc}^{-2}$ likely represent galaxies with a clumpy ISM, and the modelled and observed H_2 gas surface densities may differ in this regime.

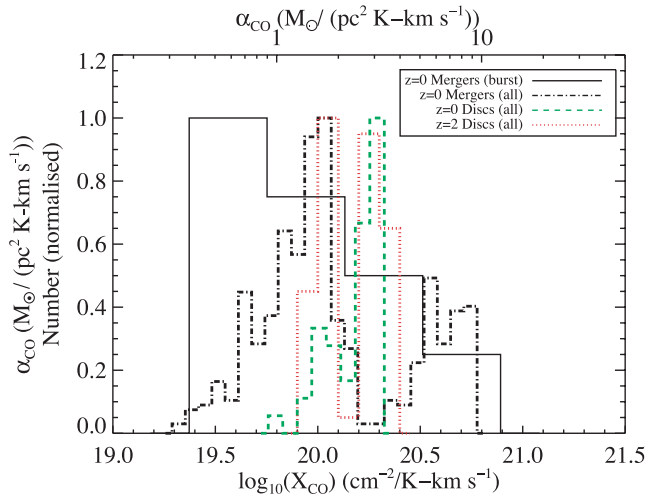


Figure 4. Distribution of X_{CO} values during the peak of the SFR (the ‘burst’ snapshot) for all 1:1 and 1:3 local galaxy mergers (black solid), all $z=0$ 1:1 and 1:3 mergers (i.e. not just the burst snapshots; black dash-dot), all high- z disc models with $Z' \approx 1$ (red dotted) and low- z disc models with $Z' \approx 1$ (green dashed). See text for details.

mergers show X_{CO} values ranging from above the Milky Way mean to an order of magnitude below it during their peak starburst. When sampling the entire library of merger orbits for a given merger mass ratio, a wide range in outcomes is apparent. We see a diverse set of velocity dispersions in the gas, as well as SFRs, owing to differing efficiencies at which angular momentum is removed from the gas. Some models undergo rather vigorous starbursts (approaching $\sim 500 M_{\odot} \text{ yr}^{-1}$), whereas others hardly sustain a noticeable starburst upon final coalescence. Galaxies that undergo their peak starburst only on first passage can have rather different metallicities in their ISM than mergers that go through a vigorous star formation period during first passage and inspiral before experiencing a starburst contemporaneous with final coalescence.

In the solid line of Fig. 4, we plot the distribution of emission-weighted mean X_{CO} values for each of our 1:1 $z=0$ merger models during the peak of their SFR. For comparison, we plot the distribution of X -factors for our $z=0$ discs in the green dashed line (only plotting galaxies with \sim solar metallicity), as well as the distribution of X_{CO} for our $z=2$ discs (which we discuss in more detail in Section 3.4). As we see, there is no ‘merger’ value for X_{CO} . It is possible to have X_{CO} values in starbursting mergers comparable to the Milky Way’s. The fact that starbursting mergers, on average, have lower X -factors than the Galactic mean is likely due to a selection effect. We return to this point in more (quantitative) detail in Section 4.

3.4 X_{CO} in high-redshift galaxies

3.4.1 Basic results

Now that we have developed intuition regarding the variation of X_{CO} with metallicity and surface density, we are in a position to understand how galaxies at high redshift may behave with respect to the CO– H_2 conversion factor.

Mergers at high z are some of the most luminous, rapidly star-forming galaxies in the Universe. As an example, many $z \sim 2$ submillimetre-selected galaxies (SMG) form stars at $\gtrsim 1000 M_{\odot} \text{ yr}^{-1}$ (Narayanan et al. 2010a). However, despite the \sim order of magnitude greater SFR in these galaxies compared to local mergers,

mergers at high z are similar to their low-redshift counterparts in terms of their typical X -factors. While the mean gas surface densities in e.g. $z \sim 2$ SMGs are larger than low-redshift mergers (e.g. Tacconi et al. 2008; Narayanan et al. 2010a), both the dust temperatures and gas velocity dispersions also rise commensurately.

As a specific example, we focus on a 1:1 major merger at $z \sim 2$ (This is model ‘z3b5e’; please refer to Table A1 in the Appendix for the initial conditions of this model merger.). Model z3b5e undergoes a luminous burst of $\sim 1500 M_{\odot} \text{ yr}^{-1}$, and may be selected as a SMG when it merges (Narayanan et al. 2009; Hayward et al. 2011). During the burst, this simulation reaches a mass-weighted mean surface density of molecular gas of $\sim 10^4 M_{\odot} \text{ pc}^{-2}$. At the same time, the mass weighted kinetic (dust) temperature is $\sim 150(160) \text{ K}$,⁴ and the mass-weighted velocity dispersion in the GMCs is $\sim 140 \text{ km s}^{-1}$. Doing a simple scaling results in a mean X_{CO} of $\sim 5 \times 10^{19} \text{ cm}^{-2}/\text{K-km s}^{-1}$. Of course, the real mass-weighted value may vary from this owing to both radiative transfer as well as the fact that this simple scaling is not a true averaging. Observational estimates of the X -factor in SMGs suggest that they are similar to the lower values in the range of local ULIRGs (Tacconi et al. 2008).

Our simulated disc galaxies at high-redshift show a range of X_{CO} values, ranging from comparable to the Galactic mean to values two to five times lower. The reason massive discs at high-redshift may have lower X -factors than the Galactic mean can be understood in the following way. In contrast to present-epoch galaxies, galaxies at higher-redshifts ($z \gtrsim 1$) at a fixed stellar mass are denser and more gas-rich (e.g. Erb et al. 2006; Förster Schreiber et al. 2009; Daddi et al. 2010b; Tacconi et al. 2010). Both simulations and observations suggest that galaxies around redshifts $z \sim 1$ – 2 may have baryonic gas fractions of order 20–60 per cent (Davé et al. 2010; Daddi et al. 2010b; Tacconi et al. 2010). A primary consequence of this is that discs at higher-redshifts may be heavily star forming, with SFRs of the order of $\sim 10^2 M_{\odot} \text{ yr}^{-1}$, comparable to local galaxy mergers (Daddi et al. 2007; Förster Schreiber et al. 2009; Narayanan et al. 2010b). In fact, simulations suggest that disc galaxies at $z \sim 2$ likely dominate the infrared luminosity function (Hopkins et al. 2010).

In the absence of rather extreme stellar feedback, very gas rich discs at high redshift can be unstable to fragmentation, and form massive \sim kpc-scale clumps (e.g. Springel et al. 2005; Ceverino, Dekel & Bournaud 2010). These clumps can have relatively high velocity dispersions ($\sim 10^2 \text{ km s}^{-1}$) and warm gas temperatures owing to high volumetric densities and high SFRs (Bournaud et al. 2010).

These effects are the strongest in the most massive discs. Our most massive $z=2$ model disc galaxy has a total baryonic mass of $\sim 5 \times 10^{11} M_{\odot} \text{ yr}^{-1}$, and has typical⁵ X -factors ranging anywhere between a factor of 5 below the Galactic mean to the Galactic mean value. The lower mass $z=2$ isolated disc models (with baryonic masses of $M_{\text{bar}} = 1 \times 10^{11}$ and $3.5 \times 10^{10} M_{\odot}$) typically have

⁴ Note that owing to radiative transfer effects, this dust temperature is not necessarily what would be derived simply by identifying the location of the peak of the SED.

⁵ Because our simulations are not cosmological, there is no accretion of intergalactic gas. As a result, the metallicities in our model galaxies only rise with time. Because the X -factor is dependent on metallicity (Section 3.2), we have to make a choice as to which snapshot/metallicity to consider as a ‘typical’ galaxy. We assume any snapshot above $Z' > 0.5$ is ‘typical’ based on the steady-state metallicities found for galaxies of baryonic mass comparable to those in our sample from cosmological modelling (fig. 2 of Davé et al. 2010, though see Keres et al. 2011; Vogelsberger et al. 2011 and Sijacki et al. 2011).

X -factors comparable to the Milky Way mean. Returning to Fig. 4, we examine the red dotted line that represents $z \sim 2$ disc models. Because the idea of a ‘starburst’ snapshot is less meaningful for the evolution of a disc galaxy, we plot the X -factor for every snapshot for our model discs with metallicities around solar. We see a large spread in mean X -factors.

3.4.2 Do mergers and discs have inherently different X -factors?

In light of the fact that high- z discs have, at times, SFRs comparable to local galaxy mergers, a pertinent question is whether there is an intrinsic difference in the X -factor between high- z discs and galaxy mergers. Another way of saying this is, for a given set of physical conditions, are the X -factors from mergers lower than the X -factors from high- z gas-rich, gravitationally unstable discs? A cursory examination of Fig. 4 indicates that mergers (the black solid line) have systematically lower X -factors than discs (the blue and red dashed and dotted lines). Indeed, in the local Universe, it is observed that mergers have, on average, lower X -factors than discs (e.g. Tacconi et al. 2008). However, this is likely due to a selection bias. We remind the reader that the black solid line in Fig. 4 represents *starbursting* mergers. These mergers are caught when their gas is extremely warm and with large velocity dispersion. When comparing mergers and discs with comparable physical conditions, the observed X_{CO} values are in fact quite similar. It is the physical conditions in a galaxy that determine the X -factor, not the global morphology.

To demonstrate this, we perform three tests. First, we compute the distribution of X_{CO} values for *all* 1:1 and 1:3 merger snapshots (at \sim solar metallicity), and indicate this with the black dot-dashed line in Fig. 4. As we see, the distribution of X_{CO} values is broad, but with substantially less power in the low X -factor regime than the distribution that denotes only starbursting mergers (black solid line). This highlights that mergers which are selected during a particularly active phase are more likely to have low X -factors, due to their warm and high- σ gas. When controlling for this effect by picking galaxies with similar CO intensity (W_{CO}) and metallicity, mergers and discs have the same X_{CO} on average.

To show this, in Fig. 5, we perform our second test in which we examine the X -factors from all the 1:1 and 1:3 mergers (at low z) and compare them to the X_{CO} from high- z discs with the same⁶ metallicity and CO intensity (W_{CO}). We could equivalently perform this analysis in terms of Σ_{H_2} , though as we will show in Section 4, parametrizing in terms of W_{CO} is desirable with regard to observations. There is a strong peak at X_{CO} ratios near unity, with some spread. The median value in the distribution is ~ 0.8 , and the mean is ~ 1.1 . The implication from Fig. 5 is that galaxies with similar physical conditions (here Z' and W_{CO}) have similar X -factors, regardless of whether they are discs or mergers. The fact that mergers, on average, have lower X -factors than discs in the local Universe likely derives from the fact that they are selected as starbursts, which have preferentially higher temperatures and velocity dispersions in the gas.

Thirdly, in Fig. 6, we examine the relationship between X_{CO} and W_{CO} for the same galaxies plotted⁷ in Figs 4 and 5. These are all galaxies with metallicities around solar. The principal result from

⁶ ‘The same’ here means that the values of Z' and W_{CO} are within 10 per cent of one another.

⁷ To reduce clutter in the plot, we randomly draw 10 per cent of the galaxies within each merger ratio bin to plot.

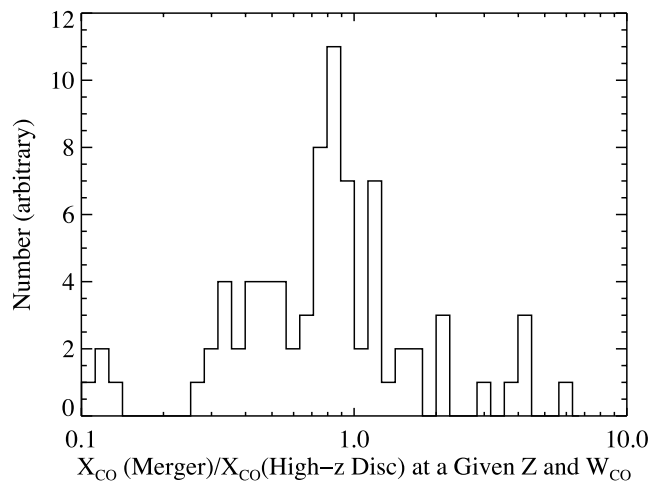


Figure 5. Comparison of the X -factor between low- z mergers (1:1 and 1:3) and high- z star-forming discs. The histogram denotes the ratio of X -factor from mergers versus high- z discs between snapshots with a similar metallicity and CO intensity. The sharp peak near unity implies that galaxies with similar physical conditions have similar X -factors, independent of large-scale morphology.

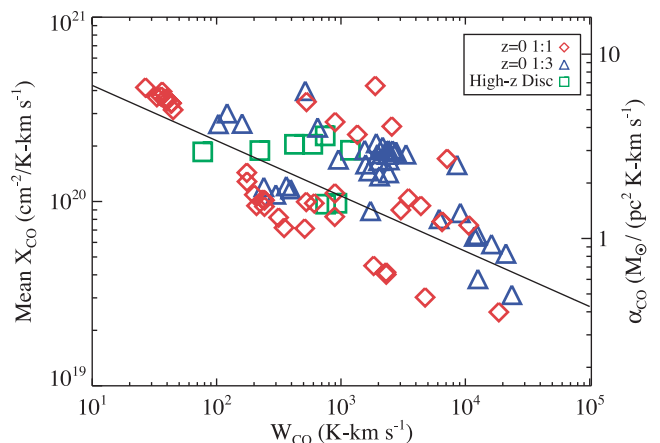


Figure 6. Comparison of X_{CO} versus CO intensity (W_{CO}) for low- z galaxy mergers and high- z discs in an effort to investigate if mergers and discs inherently have different X_{CO} properties. Included in this plot are all 1:1 and 1:3 mergers simulated at $z=0$. Only snapshots with metallicities $Z' > 0.7$ are shown. To reduce clutter in the plot, we plot only a randomly drawn subsample (10 per cent) of the snapshots from each mass ratio. The line shows the best fit from equation (8). Evidently, galaxies that have similar physical conditions have similar X -factors, independent of galaxy morphology or evolutionary history. See text for details.

Fig. 6 is that galaxies within a relatively limited metallicity and W_{CO} (or surface-density) range have similar X -factors, regardless of the type of merger it is. Mergers and discs have similar X_{CO} values when they have similar physical conditions, and are not inherently different based on their global morphology. In addition, Fig. 6, like Figs 2 and 3, shows a systematic decrease of X_{CO} with increasing W_{CO} (and Σ_{mol}).

4 APPLICATION TO OBSERVATIONS

4.1 Deriving X_{CO} from observations

As we have seen from the previous sections, it is clear that there is a continuum of X_{CO} values that vary with galactic environment. The dominant drivers of the X -factor in our simulations are the metallicity of the star-forming gas, and the thermal and dynamical state of the GMCs. Informed by this, we are motivated to parametrize X_{CO} as a function of observable properties of galaxies.

Metallicity is a crucial ingredient to any parametrization. At sub-solar metallicities, we see the rapid growth of CO-dark GMCs. This has been noted both in observations (e.g. Leroy et al. 2011; Genzel et al. 2012) and in other numerical models (Feldmann, Gnedin & Kravtsov 2011; Krumholz, Leroy & McKee 2011; Shetty et al. 2011b). As we saw in Section 3.2, as well as in Fig. 3, at a given galaxy surface density (or CO intensity), X_{CO} increases with decreasing metallicity.

Beyond this, as was shown in Section 3.3, as well as in the models of Narayanan et al. (2011b), galaxy surface density is correlated with the thermal and dynamical state of the gas: at a given metallicity, higher surface density galaxies, on average, correspond to galaxies with a warm and high velocity dispersion molecular ISM, due to their higher SFRs.

Informed by these results, we perform a 2D Levenberg–Marquardt fit (Marquardt 2009) on our model galaxies (considering every snapshot of every model), fitting X_{CO} as a function of mass-weighted mean metallicity and mass-weighted mean H_2 surface density. We find that our simulation results are reasonably well fitted by a function of the form:

$$X_{\text{CO}} \approx \frac{1.3 \times 10^{21}}{Z' \times \langle \Sigma_{\text{H}_2} \rangle^{0.5}} \quad (6)$$

where Σ_{H_2} is in units of $\text{M}_{\odot} \text{pc}^{-2}$ and X_{CO} is in units of $\text{cm}^{-2}/\text{K-km s}^{-1}$. Equation (6) provides a good fit to the model results above metallicities of $Z' \approx 0.2$. Turning again to Figs 1, 2, 3 and 6, we highlight the solid lines which show how equation (6) fits both the simulation results and observational data. We note that Ostriker & Shetty (2011) obtained a similar result, $\alpha_{\text{CO}} \propto \Sigma_{\text{mol}}^{-0.5}$, by interpolating between empirical α_{CO} values ($\alpha_{\text{CO}} = 3.2$ for $\Sigma_{\text{mol}} = 100 \text{ M}_{\odot} \text{pc}^{-2}$ and $\alpha_{\text{CO}} = 1$ for $\Sigma_{\text{mol}} = 1000 \text{ M}_{\odot} \text{pc}^{-2}$).

Because Σ_{H_2} is not directly observable (hence the need for an X -factor), we re-cast equation (6) in terms of the velocity-integrated CO line intensity. In order to parametrize X_{CO} in a manner that is independent of the effects of varying beam-sizes or observational sensitivity, we define the observable CO line intensity as the luminosity-weighted CO intensity over all GMCs, i :

$$\langle W_{\text{CO}} \rangle = \frac{\int W_{\text{CO}}^2 dA}{\int W_{\text{CO}} dA} \equiv \frac{\sum L_{\text{CO},i} \times W_{\text{CO},i}}{\sum L_{\text{CO},i}} \quad (7)$$

where $\langle W_{\text{CO}} \rangle$ is in units of K-km s^{-1} , and is the CO surface brightness of the galaxy. We then fit to obtain a relation between X_{CO} , Z' and $\langle W_{\text{CO}} \rangle$:

$$X_{\text{CO}} = \frac{6.75 \times 10^{20} \times \langle W_{\text{CO}} \rangle^{-0.32}}{Z'^{0.65}} \quad (8)$$

where again $\langle W_{\text{CO}} \rangle$ is CO line intensity measured in K-km s^{-1} , X_{CO} is in $\text{cm}^{-2}/\text{K-km s}^{-1}$ and Z' is the metallicity divided by the solar metallicity. By converting X_{CO} to α_{CO} , we similarly obtain:

$$\alpha_{\text{CO}} = \frac{10.7 \times \langle W_{\text{CO}} \rangle^{-0.32}}{Z'^{0.65}} \quad (9)$$

where α_{CO} is in units of $\text{M}_{\odot} \text{pc}^{-2} (\text{K-km s}^{-1})^{-1}$.

It is important to recognize that the power law in equation (8) cannot describe X_{CO} indefinitely. At very low W_{CO} , GMCs tend towards fixed properties in galaxies and the galactic environment plays a limited role in setting X_{CO} . Considering this, equation (8) formally becomes

$$X_{\text{CO}} = \frac{\min [4, 6.75 \times \langle W_{\text{CO}} \rangle^{-0.32}] \times 10^{20}}{Z'^{0.65}} \quad (10)$$

or, similarly:

$$\alpha_{\text{CO}} = \frac{\min [6.3, 10.7 \times \langle W_{\text{CO}} \rangle^{-0.32}]}{Z'^{0.65}}. \quad (11)$$

Equations (10) and (11) can be used directly with observations of galaxies to infer an expected X -factor. One advantage of this formalism is that it captures the continuum of CO– H_2 conversion factors, rather than utilizing bimodal ‘disc’ and ‘ULIRG’ values. Because we have chosen the physical quantities in our modelling based on mass or luminosity-weighted averages, they are defined without reference to a particular scale. Consequently, equation (10) can be used on scales ranging from our resolution limit of $\sim 70 \text{ pc}$ to unresolved observations of galaxies.

It is conceivable that alternative definitions of the observed mean CO intensity could be appropriate. One can imagine implementing an area-weighted intensity, i.e. $W_{\text{CO}} = L_{\text{CO}}/\text{Area}$. This has the undesirable attribute of being dependent on a defined scale.

4.2 The Kennicutt–Schmidt star formation relation in galaxies from $z=0$ to 2

A natural application of our model for the CO– H_2 conversion factor is the KS SFR surface density–gas surface density relation in galaxies. Because the inferred H_2 gas masses from observed galaxies are inherently dependent on conversions from CO line intensities, our understanding of the KS relation is fundamentally tied to the potential variation of X_{CO} with the physical environment in galaxies.

Recent surveys of both local galaxies (e.g. Kennicutt 1998a,b; Bigiel et al. 2008, and references therein) and pioneering efforts at higher redshifts (e.g. Bouché et al. 2007; Bothwell et al. 2010; Daddi et al. 2010a; Genzel et al. 2010) have provided a wealth of data contributing to our knowledge of the star formation relation in both quiescent disc galaxies and starbursts. Work by Daddi et al. (2010a) and Genzel et al. (2010) demonstrate the sensitivity of these relations to the CO– H_2 conversion factor: when applying the traditional bimodal conversion factor ($X_{\text{CO}} \approx 8 \times 10^{19} \text{ cm}^{-2}/\text{K-km s}^{-1}$ for ULIRGs and $X_{\text{CO}} \approx 2 \times 10^{20} \text{ cm}^{-2}/\text{K-km s}^{-1}$ for discs) to the starburst galaxies and discs, respectively, a bimodal SFR relation becomes apparent when the data are plotted in terms of Σ_{SFR} and Σ_{mol} .

In Figs 7–9, we illustrate the effects of our model fit for X_{CO} as a function of galaxy physical properties. In the left-hand panel of Fig. 7, we plot the SFR surface density for both local galaxies and high- z galaxies as compiled by Daddi et al. (2010a) and Genzel et al. (2010) against their CO line intensity, W_{CO} . Although there is significant scatter, the Σ_{SFR} versus W_{CO} relation is unimodal. In the middle panel, we plot the SFR– Σ_{H_2} relation utilizing the bimodal X -factors assumed in the literature [with the above ‘ULIRG’ value for the inferred mergers (local ULIRGs and high- z SMGs), and the above ‘quiescent’ value for low- z discs and high- z BzK galaxies].⁸

⁸ In practice, for the high- z BzK galaxies, we utilize an X -factor of $X_{\text{CO}} \approx 2.3 \times 10^{20} \text{ cm}^{-2}/\text{K-km s}^{-1}$ to remain consistent with Daddi et al. (2010a), though the usage of this versus the more standard disc value makes little difference.

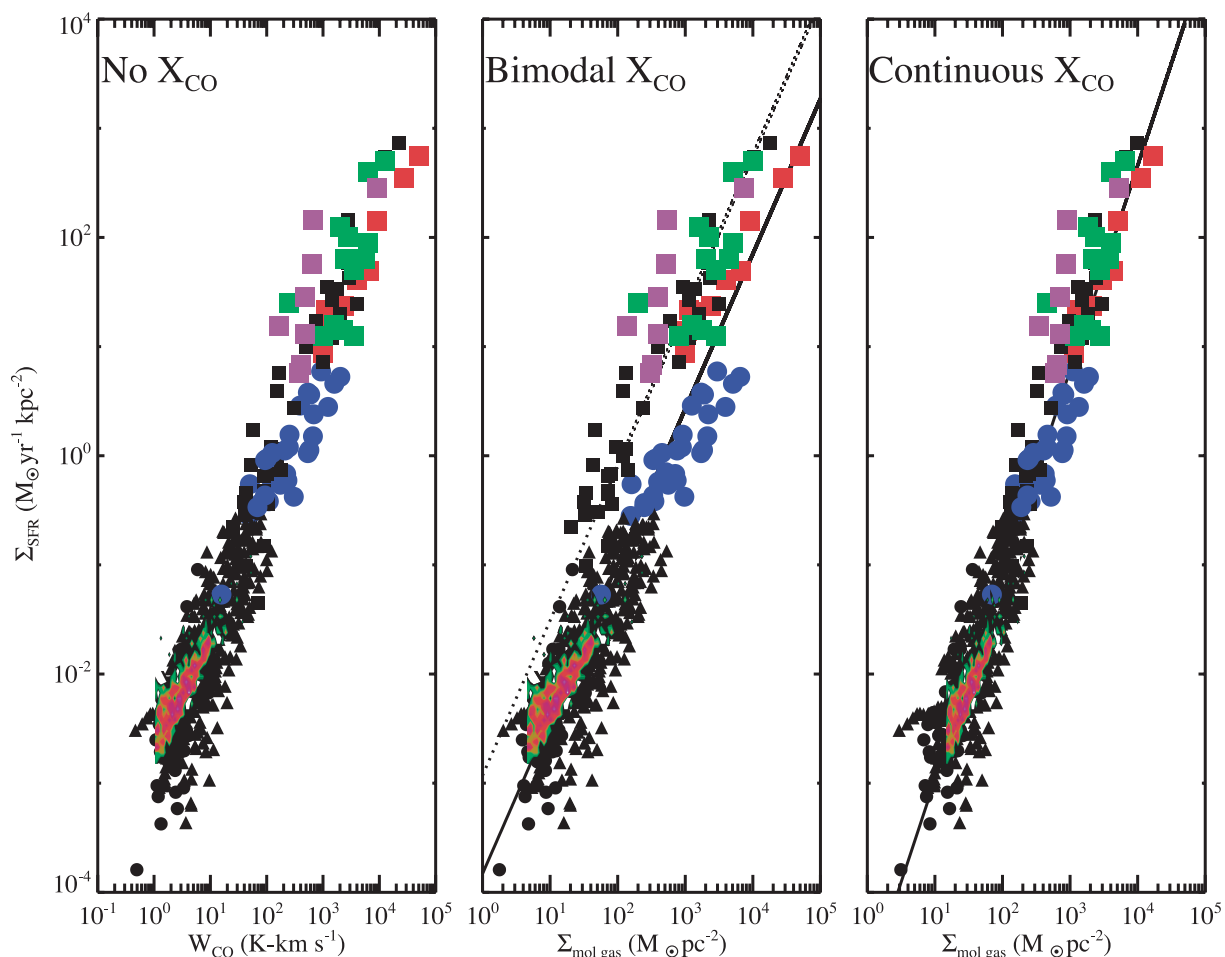


Figure 7. KS star formation relation (SFR surface density versus H_2 gas surface density) in observed galaxies. Circles and triangles are local discs or high- z BzK galaxies, and squares are inferred mergers (local ULIRGs or high- z SMGs). Colours denoting separate surveys are described below. Left: SFR surface density versus velocity-integrated CO intensity, yielding a unimodal SFR relation. Centre: when applying an effectively bimodal X_{CO} ($\alpha_{\text{CO}} = 4.5$ for local discs, 3.6 for high- z discs and 0.8 for mergers), the resulting SFR relation is bimodal. The solid and dotted lines overplotted are the best-fitting tracks for each ‘mode’ of star formation as in Daddi et al. (2010a). Right: SFR relation when applying equation (10) to the observational data, resulting in a unimodal SFR relation. The power-law index in the relation is approximately 2 (solid line). Symbol legend: we divide galaxies into ‘disc-like’ with filled circles, and ‘merger-like’ with squares. This assumes that high- z BzK galaxies are all discs, high- z SMGs and low- z ULIRGs are all mergers. The low- z disc observations (black filled circles and black triangles) come from Kennicutt et al. (2007), Wong & Blitz (2002), Crosthwaite & Turner (2007), Schuster et al. (2007) and comprise both resolved and unresolved points. The resolved points from the survey of Bigiel et al. (2008) are denoted by the coloured contours. The local ULIRGs are compiled by Kennicutt (1998b) and are denoted by black filled squares. The high- z discs come from Genzel et al. (2010), Daddi et al. (2010a,b) and are represented by filled blue circles. The high- z SMGs are divided into the samples of Bothwell et al. (2010) (purple), Bouché et al. (2007) (green) and Greve et al. (2005), Tacconi et al. (2006; 2008), Engel et al. (2010) as compiled by Genzel et al. (2010) (filled red squares).

The circles are unresolved observations of disc galaxies at low and high z , triangles and contours are resolved observations of local discs, and the squares are local ULIRGs and inferred mergers at high-redshift. When separate high and low values of X_{CO} are adopted for discs and mergers, a bimodal relationship between Σ_{SFR} and Σ_{gas} results, with power-law index ranging between unity and 1.5.

In the right-hand panel of Fig. 7, we apply equation (10) to the observational data (assuming $Z' = 1$ for the galaxies). The scatter in the modified relation immediately tightens, and it becomes unimodal. To numerically quantify the reduction in scatter with the modified relation we examine the ratio of the maximum inferred Σ_{H_2} to the minimum for all points within the relatively tight SFR surface density range of $[0.05, 0.1] \text{ M}_{\odot} \text{ yr}^{-1} \text{ kpc}^{-2}$ for the centre and right-hand panels of Fig. 7. The scatter is reduced by approximately

a factor of 5. Within this Σ_{SFR} range, no mergers are in the sample. Thus, the reduction in scatter is not due to simply using a unimodal X_{CO} versus bimodal X_{CO} . We note that in applying equation (10) to the observed data, we have to assume that the intensity within the reported area is uniform. If the emission is instead highly concentrated over very few pixels, then the application of equation (10) may overestimate X_{CO} .

The reason for the transition from a bimodal to unimodal KS relation is clear. In the modified relation, similar to the traditional KS plot that uses a bimodal X -factor, the lower luminosity discs have CO– H_2 conversion factors comparable to the Galactic mean, and the most luminous discs have X -factors up to an order of magnitude lower. Very massive, gas-rich, unstable discs, as well as lower luminosity mergers, have X -factors in between the two, however, and fill in the continuum. Utilizing equation (10), a simple linear

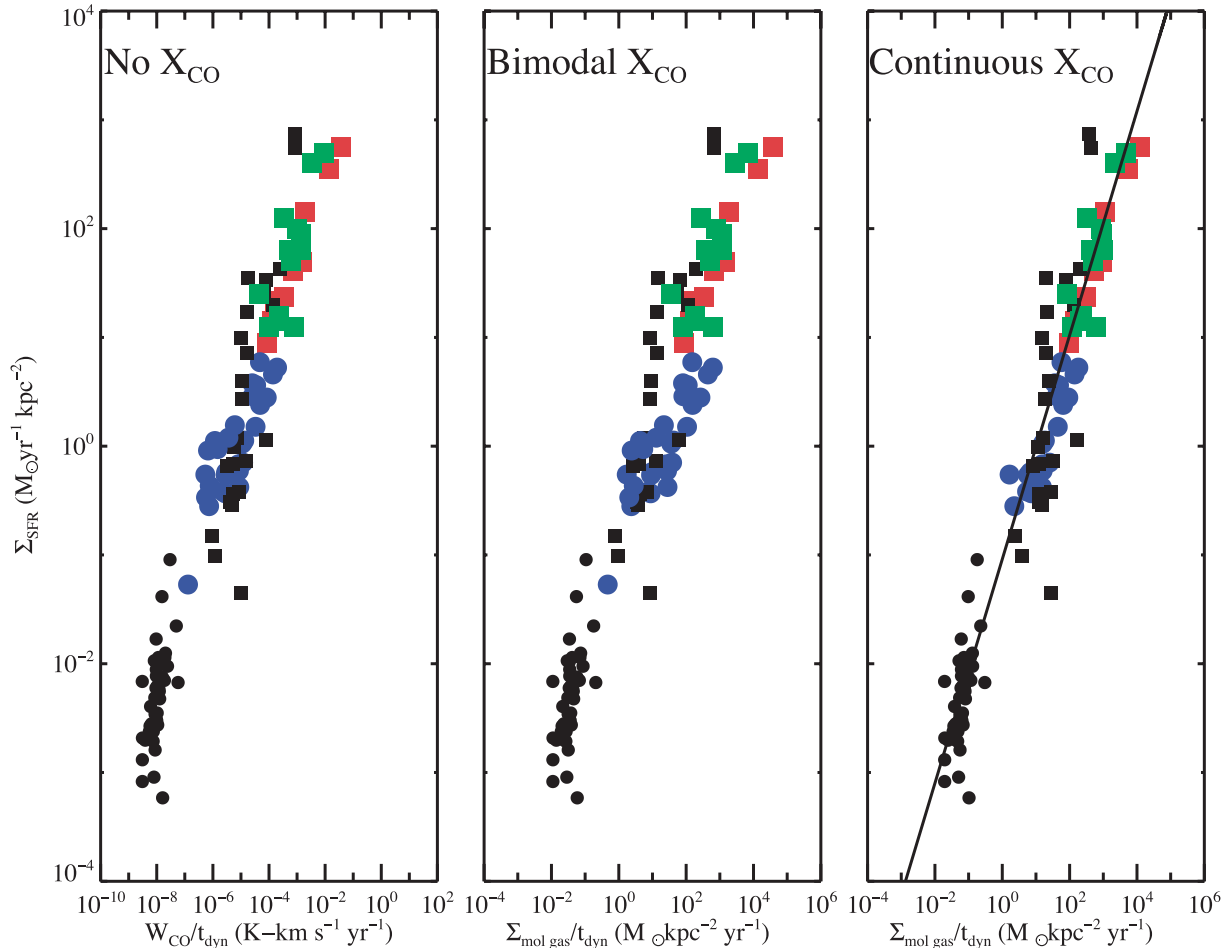


Figure 8. Similar to Fig. 7, but with the abscissa showing W_{CO} or Σ_{mol} divided by the orbital time of the observed galaxy. Symbols are the same as in Fig. 7, but we omit galaxies for which orbital times are not available. The best-fitting slope in the right-hand panel is of the order of unity. See text for details.

chi-square fit of the observed data on the right-hand side of Fig. 7 returns:

$$\log_{10}(\Sigma_{\text{SFR}}) = 1.95 \times \log_{10}(\Sigma_{\text{mol}}) - 4.9 \quad (12)$$

where Σ_{SFR} is measured in $M_{\odot} \text{ yr}^{-1} \text{ kpc}^{-2}$ and Σ_{mol} is measured in $M_{\odot} \text{ pc}^{-2}$. Utilizing an empirical method to obtain $X_{\text{CO}} \propto W_{\text{CO}}^{-0.3}$, Ostriker & Shetty (2011) previously showed that the observational data compiled in Genzel et al. (2010) yield a similar fit to equation (12).

We remind the reader of the assumptions that have gone into this fit: we have assumed that every galaxy has solar metallicity, and neglected any potential effects of differential excitation in the CO as a function of infrared luminosity (e.g. Narayanan et al. 2011a). Nevertheless, the application of a variable X -factor on the SFR–gas surface density relation has interesting implications.

First, the index of ~ 2 of equation (12) is consistent with the analytic models and hydrodynamic simulations of self-regulated star formation by Ostriker & Shetty (2011). This work suggests that in molecular regions where supernova-driven turbulence controls the SFR and gas dominates the vertical gravity, the SFR surface density should be proportional to the gas surface density squared: $\log(\Sigma_{\text{SFR}}) = 2 \times \log(\Sigma_{\text{mol}}) - 5.0$ [adopting fiducial parameters in equation (13) of Ostriker & Shetty (2011)]. This is shown as the solid line in the right-hand panel of Fig. 7, and is very comparable to the best-fitting relation. Secondly, comparing equation (12) to

equation (13) of Ostriker & Shetty (2011), the empirical results are consistent with a value of momentum injected/total stellar mass formed of $f_p \times p_*/m_* \sim 3000 \text{ km s}^{-1} (\Sigma_{\text{mol}}/100 M_{\odot} \text{ pc}^{-2})^{-0.05}$; the fiducial value adopted in Ostriker & Shetty (2011) is 3000 km s^{-1} .

Daddi et al. (2010a) and Genzel et al. (2010) suggest an alternative mechanism for reducing the scatter imposed by the utilization of a bimodal X_{CO} in Fig. 7. Specifically, these authors find that by dividing the molecular gas surface density by the galaxy’s orbital time, the observed KS relation goes from bimodal to unimodal, suggesting that the galaxy’s global properties are related to the local, small-scale processes of star formation. That is to say, when using a bimodal X_{CO} , the $\Sigma_{\text{SFR}} - \Sigma_{\text{mol}}$ relationship is bimodal, whereas the $\Sigma_{\text{SFR}} - \Sigma_{\text{mol}}/t_{\text{dyn}}$ relationship is unimodal, with some scatter.

If one abandons the bimodal X_{CO} approximation, and utilizes our favoured model for X_{CO} , the observed relationship between Σ_{SFR} and $\Sigma_{\text{mol}}/t_{\text{dyn}}$ remains unimodal, and in fact the scatter in the relation is reduced compared to what one obtains using a bimodal X_{CO} . To show this, in Fig. 8, we show the analogue to Fig. 7, but with the abscissa showing the surface density or W_{CO} divided by the dynamical time. The dynamical times used are the same as those in Daddi et al. (2010a) and Genzel et al. (2010), and are defined as the rotational time at either the galaxy’s outer radius, or half-light radius, depending on the sample. In the left-hand panel of Fig. 8, we show the relationship between Σ_{SFR} and $W_{\text{CO}}/t_{\text{dyn}}$ (i.e. pure

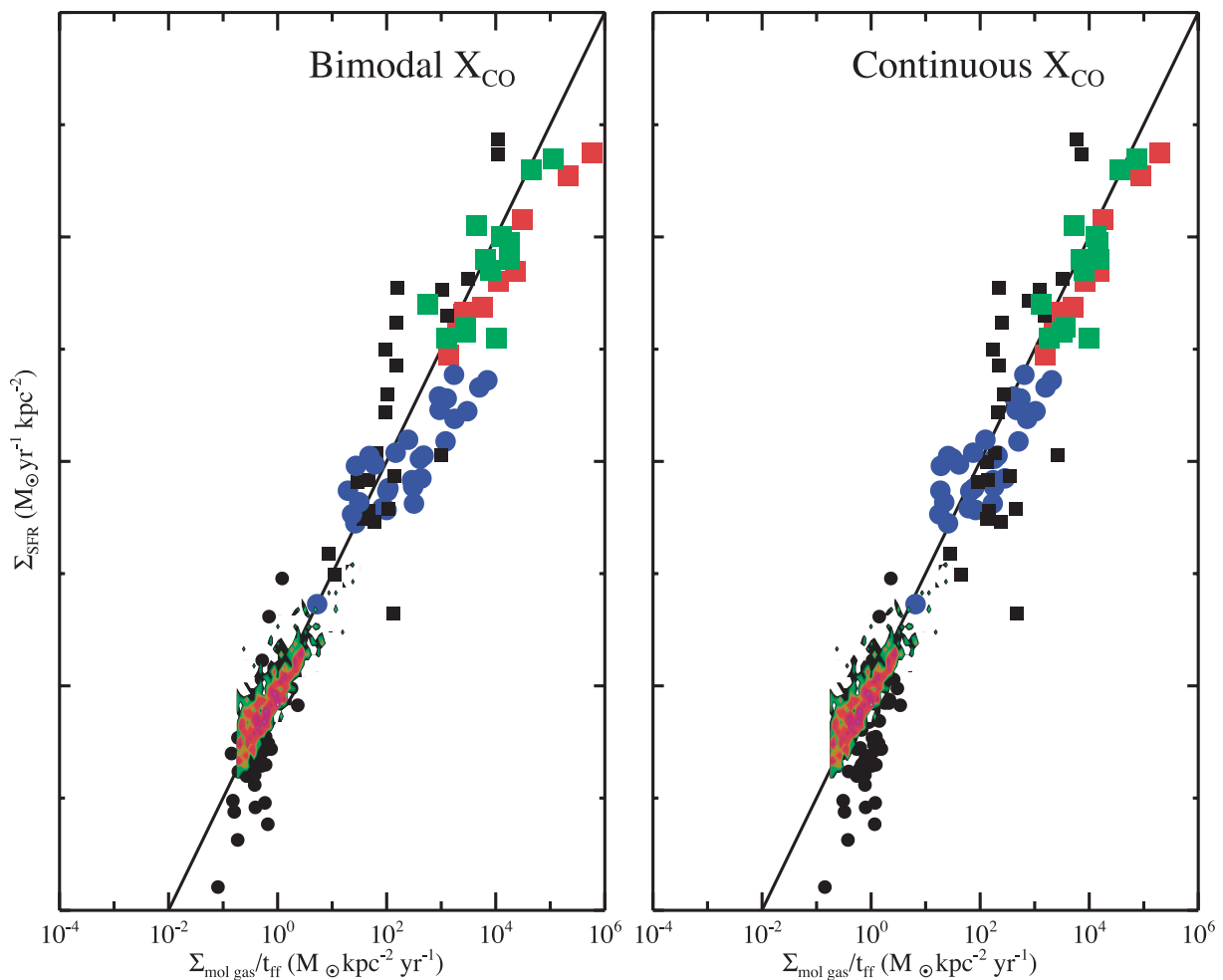


Figure 9. Same as Fig. 7, but instead of plotting Σ/t_{dyn} on the abscissa we instead plot Σ/t_{ff} , where t_{ff} is the free-fall time in the star-forming clouds of a galaxy – see main text for details. We do not include a $\Sigma_{\text{SFR}} - W_{\text{CO}}/t_{\text{ff}}$ plot as the calculation of t_{ff} requires a gas mass. Symbols are the same as in Figs 7 and 8. The left-hand panel shows the results using a bimodal X_{CO} , while the right-hand panel shows the results using our continuous X_{CO} . The solid black lines show the relation $\Sigma_{\text{SFR}} = \epsilon_{\text{ff}} \Sigma_{\text{mol}}/t_{\text{ff}}$ with $\epsilon_{\text{ff}} = 0.01$.

observables); in the centre panel, we show the relationship between Σ_{SFR} and $\Sigma_{\text{mol}}/t_{\text{dyn}}$ when assuming a bimodal X_{CO} [as is done in Daddi et al. (2010a) and Genzel et al. (2010)] and in the right-hand panel we show the same relationship, but with Σ_{mol} determined using our best-fitting continuous X_{CO} , rather than the bimodal X_{CO} value used in Daddi et al. (2010a) and Genzel et al. (2010). We find a best-fitting relation (using our model for X_{CO}) of

$$\log_{10}(\Sigma_{\text{SFR}}) = 1.03 \times \log_{10}(\Sigma_{\text{mol}}/t_{\text{dyn}}) - 1.05 \quad (13)$$

where Σ_{SFR} and $\Sigma_{\text{mol}}/t_{\text{dyn}}$ are both in $M_{\odot} \text{ yr}^{-1} \text{ kpc}^{-2}$.

Our best-fitting $\Sigma_{\text{SFR}} - \Sigma_{\text{mol}}/t_{\text{dyn}}$ relation has a slope of approximately unity, comparable to what is found by Genzel et al. (2010), and consistent with the best-fitting slope of Daddi et al. (2010a) of ~ 1.15 . A principal difference between using our model X_{CO} versus the bimodal X_{CO} in calculating the $\Sigma_{\text{SFR}} - \Sigma_{\text{mol}}/t_{\text{dyn}}$ relation is a reduction of scatter. When measuring the scatter near SFR surface density of $1 M_{\odot} \text{ yr}^{-1} \text{ kpc}^{-2}$, we find that using our model X_{CO} versus the bimodal value reduces the scatter by a factor of ~ 5 .

The fact that our model for the $\Sigma_{\text{SFR}} - \Sigma_{\text{mol}}/t_{\text{dyn}}$ relation is consistent with the observed one (though with reduced scatter) is not surprising. Daddi et al. (2010a) and Genzel et al. (2010) assume a Milky Way like X_{CO} for their disc galaxies, and roughly a fac-

tor of 5 lower for their mergers. In our model, the assumption of a bimodal X_{CO} for discs and mergers is correct on average. The mean value for X_{CO} for high- z SMGs and low- z mergers is in fact lower than the mean value for local discs (cf. Section 4.3). However, many galaxies lie in the overlap region. Some local ULIRGs have X -factors comparable to the Galactic average, and some high- z discs have X -factors more similar to the canonical literature ‘merger value’. By modelling the continuous nature of X_{CO} and more properly treating these intermediate cases, a reduction in scatter is natural.

Finally, we consider Σ_{SFR} as a function of $\Sigma_{\text{mol}}/t_{\text{ff}}$, where t_{ff} is the free-fall time within the dense molecular star-forming clouds in the galaxy. Both observations and theory have suggested that the star formation efficiency per free-fall time ϵ_{ff} in molecular gas is approximately constant (Krumholz & McKee 2005; Krumholz & Tan 2007; Evans et al. 2009; Ostriker & Shetty 2011; Krumholz, Dekel & McKee 2012). We infer t_{ff} from the observable properties of the galaxy (using the approximations of Krumholz et al. 2012), together with either a bimodal X_{CO} or our favoured continuous X_{CO} . Krumholz et al. show that using t_{ff} rather than t_{dyn} makes it possible to fit the unresolved extragalactic observations, the resolved observations of Local Group galaxies from Bigiel et al. (2008) and

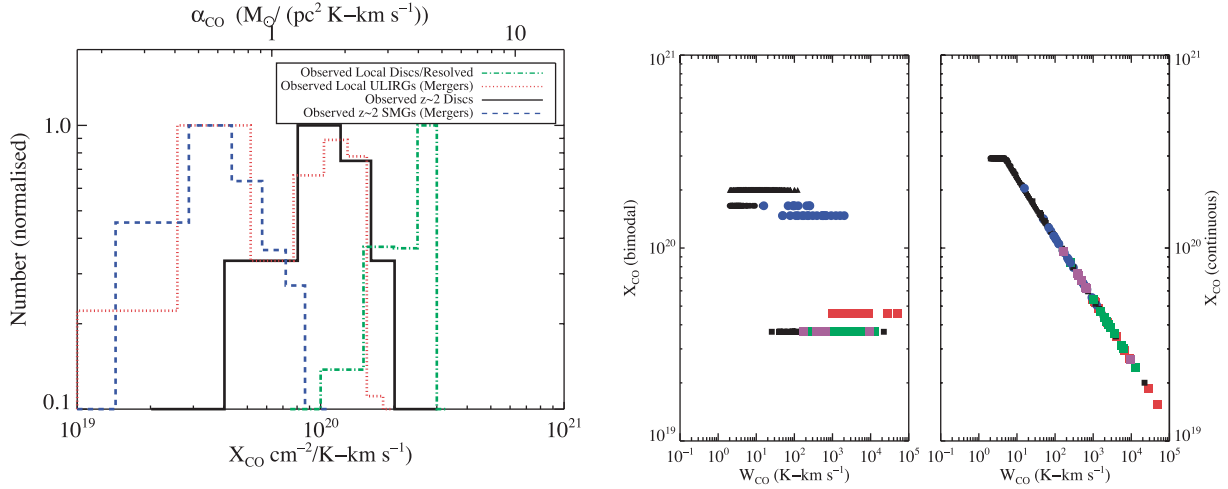


Figure 10. Left: we utilize our model fit for X_{CO} (equation 10) to infer the X_{CO} values for observed galaxies compiled by Genzel et al. (2010) and Daddi et al. (2010a). Right: CO line intensity, W_{CO} versus X_{CO} for the observed galaxies from Fig. 7 (the colour coding of the points is the same as in Fig. 7). The X_{CO} values are both the original literature values [denoted by ‘ X_{CO} (bimodal)’] and our derived values [denoted by ‘ X_{CO} (continuous)’].

individual molecular clouds in the Milky Way on a single relation, as illustrated in the left-hand panel of Fig. 9. The right-hand panel of the figure shows that this remains true for our favoured X_{CO} and that a star formation law $\Sigma_{\text{SFR}} = \epsilon_{\text{ff}} \Sigma_{\text{mol}} / t_{\text{ff}}$ with $\epsilon_{\text{ff}} \approx 0.01$ remains a good fit to the observational data. As with the $\Sigma_{\text{SFR}} - \Sigma_{\text{mol}} / t_{\text{dyn}}$ relation, using our continuous X_{CO} actually reduces the scatter, and for the same reason: our favoured X_{CO} produces essentially the same result as the traditional bimodal X_{CO} for galaxies at the extremes of the disc and merger sequences, but makes the behaviour of X_{CO} continuous rather than discontinuous for the large number of galaxies in the overlap region.

The results from Fig. 9 are compatible with the model of Ostriker & Shetty (2011). For a disc in vertical hydrostatic equilibrium with gravity dominated by the gas, and vertical velocity dispersion, v_z ,

$$\Sigma_{\text{SFR}} = \epsilon_{\text{ff}} \Sigma_{\text{SFR}} / t_{\text{ff}} = \epsilon_{\text{ff}} \times 4G \Sigma_{\text{mol}}^2 / (\sqrt{3} v_z) \quad (14)$$

(Ostriker & Shetty 2011, equation 21). Comparing to the fit obtained in equation (12) using our continuous X_{CO} relation, we find that $\epsilon_{\text{ff}} / v_z = 0.001 (\text{kms}^{-1})^{-1} (\Sigma_{\text{mol}} / 100 M_{\odot} \text{pc}^{-2})^{-0.05}$. If $v_z \approx 10 \text{ kms}^{-1}$ on small scales in the dense neutral gas, as suggested by Ostriker & Shetty (2011), this implies $\epsilon_{\text{ff}} \approx 0.01$, the value proposed by Krumholz & McKee (2005) and Krumholz & Tan (2007) and found in Fig. 9. In the self-regulation theory of Ostriker & Shetty (2011), $v_z / \epsilon_{\text{ff}} \sim (1/3) f_p \times p_* / m_*$, so that v_z and ϵ_{ff} vary together for a given momentum feedback level.

4.3 Observational constraints on the model and X_{CO} values for observed galaxies

In order to assess the validity of our parametrization of X_{CO} (equation 10), it is worth comparing our models to the existing observational constraints in the literature.

As discussed in Section 1, galaxy mergers at low redshift appear to have a range of X_{CO} values, from roughly an order of magnitude below the Galactic mean to comparable to the Milky Way average (Solomon et al. 1997; Downes & Solomon 1998; Bryant & Scoville 1999), though on average the X -factor from local ULIRGs is observed to be below the Galactic mean (Tacconi et al. 2008). At higher redshifts, the constraints on X_{CO} from inferred mergers (typically submillimetre-selected galaxies) come from either dynamical

mass modelling (Tacconi et al. 2008), or dust to gas ratio arguments (Magdis et al. 2011). The inferred X -factors from high- z SMGs also appear to be lower than the Galactic mean by a factor of ~ 5 .

There are relatively fewer constraints on X_{CO} from high- z discs. Daddi et al. (2010b) estimated the dynamical masses for resolved CO observations of high- z BzK disc galaxies. After subtracting off the measured stellar and assumed dark matter masses, they were able to derive an X_{CO} factor by relating the remaining (presumably H_2) mass to the observed CO luminosity. This method recovered a mean X -factor $\sim 2 \times 10^{20} \text{ cm}^{-2} / \text{K-km s}^{-1}$. This is consistent with the calculation of X_{CO} via dust to gas ratio arguments for a different BzK galaxy by Magdis et al. (2011).

In order to investigate how our inferred X -factors for observed galaxies (utilizing our model fit) compare to these determinations, on the left-hand side of Fig. 10, we apply equation (10) to the observed data from Fig. 7, and plot the derived X_{CO} for observed galaxies, binning separately for local ULIRGs, inferred $z \sim 2$ discs, and inferred $z \sim 2$ mergers. First, as a consistency check, we examine the inferred X -factors employing equation (10) from local disc observations, and denote this by the green dash-dotted line in Fig. 10. As expected, the derived X -factors from local discs form a relatively tight distribution around the Galactic mean value of $2\text{--}4 \times 10^{20} \text{ cm}^{-2} / \text{K-km s}^{-1}$.

From Fig. 10, it is evident that observed SMGs have extremely low X -factors, with the bulk of them a factor of a few lower than the Galactic mean value. Observed ULIRGs show a large population of galaxies with lower X_{CO} values, with a few approaching the Galactic mean. This is reasonably consistent with the range of values reported by Solomon et al. (1997), Downes & Solomon (1998) and Bryant & Scoville (1999).

As mentioned, there are far fewer constraints on X_{CO} from high- z discs, with the only constraints placing the X -factors near the Galactic mean value. The values for some of the observed galaxies in Fig. 10 are consistent with these determinations. This said, there is a peak in our inferred X -factors for high- z discs at values in-between present-epoch ULIRG X -factors and the Galactic mean value. Our models therefore predict that attempts to derive X_{CO} for a larger sample of $z \sim 2$ disc galaxies will indeed identify some that have X -factors more comparable to local ULIRGs. This means that the true H_2 gas masses from observations of high- z discs and

BzK galaxies may be lower than the values reported in the literature, though by factors of no more than ~ 2 , depending on the assumed X -factor.

Finally, on the right-hand side, we plot the CO line intensity, W_{CO} versus both the original assumed X_{CO} values for these observed galaxies, as well as our derived values. The purpose of this plot is to show how different galaxy populations are moving between the centre and right-hand panels of Fig. 7. Again, by and large, the mergers at present epoch and $z \sim 2$ tend to keep derived X -factors lower than the Galactic mean, though there are some that fall to intermediate values.

5 DISCUSSION OF OUR MODEL IN THE CONTEXT OF OTHER MODELS AND EMPIRICAL RESULTS

A number of groups have begun to address problems related to the CO–H₂ conversion factor in a variety of astrophysical environments. As such, in order to build a more complete theoretical picture of X_{CO} , it is worthwhile understanding how our models fit in with respect to these models. The methodologies vary from fully numerical to empirical.

Glover et al. (2010) and Glover & Mac Low (2011) developed magnetohydrodynamic models of GMC evolution with time-dependent chemistry to follow the formation and destruction of both H₂ and CO. These models showed that H₂ can survive even in the presence of a photodissociating radiation field at relatively low column densities owing to self-shielding, whereas CO can be destroyed more easily.

These models were expanded by Shetty et al. (2011a,b) who coupled the simulations of Glover & Mac Low (2011) to large velocity gradient radiative transfer calculations. Shetty et al. found that model GMCs with mean densities, temperatures and metallicities comparable to Galactic clouds result in X -factors comparable to the Galactic mean value of $\sim 2\text{--}4 \times 10^{20} \text{ cm}^{-2}/\text{K km s}^{-1}$. Similarly, these authors found that low-metallicity GMCs result in X -factors larger than the Galactic mean. These results are similar to what we have found in this study, and have a similar physical reasoning: in low-metallicity regions in their model GMCs, background UV photons photodissociate CO molecules while the H₂ self-shields to survive.

In the large Σ_{H_2} regime, our X_{CO} results and those of Shetty et al. (2011a,b) differ. Along lines of sight with high-surface density, Shetty et al. (2011b) show that, due to line saturation, X_{CO} begins to rise (see their fig. 2). While there is quite a bit of dispersion between model galaxies, we generically see a decrease in mean X_{CO} at high gas surface densities. The differences in X_{CO} are a consequence of differing underlying models. Shetty et al. (2011b) model individual GMCs that are resolved on sub-parsec scales, whereas our models are of entire galaxies of entire GMCs resolved at best to ~ 70 pc. In our simulations, galaxies with higher average mean GMC surface densities also typically have larger gas temperatures and velocity dispersions as was discussed in Section 3.3. The velocity dispersions in the molecular gas often owe to the turbulence driven in a galaxy merger, and are larger than would be expected if the line widths were solely due to the virial velocity of the cloud. Similarly, increased SFRs in the high surface density gas drive warmer dust, and consequently gas, temperatures. The increased temperatures and velocity dispersion allow for larger CO line intensities per unit H₂ gas mass in this scenario. In contrast, surface density variations in the GMCs of Shetty et al. (2011b) do not necessarily correlate with larger velocity dispersions and temperatures in the same

way as in a simulated galaxy merger. Thus the divergent results in the high Σ_{H_2} regime owe to different physical processes being modelled.

More recently, Feldmann et al. (2011) have studied the CO–H₂ conversion factor on galaxy-wide scales by coupling the GMC models of Glover et al. (2010) and Glover & Mac Low (2011) with post-processed cosmological hydrodynamic simulations of galaxy evolution. While Feldmann et al. do not have direct information regarding the velocity dispersion and line widths (and thus refrain from modelling environments such as ULIRGs), because they utilize the chemical reaction networks of Glover et al. (2010) and Glover & Mac Low (2011), they are able to study the effects of metallicity on the X -factor with explicit numerical simulations (rather than the semi-analytic model fit employed here). Despite their somewhat more sophisticated treatment of CO formation, the results they obtain are essentially identical to ours: in low-metallicity disc galaxies, the X -factor scales as Z' to a power between -0.4 and -0.7 , consistent with our best-fitting parametrization in equation (10).

Beyond this, Feldmann et al. relate X_{CO} to Σ_{H_2} , and find variations with scale. On large scales, they find little relationship between X_{CO} and Σ_{H_2} , whereas on smaller scales, X_{CO} increases with Σ_{H_2} . The reasons for this apparent discrepancy between the models of Feldmann et al. and ours are the same as in the discussion regarding the models of Shetty et al. (2011b).

Finally, Obreschkow & Rawlings (2009) applied a Bayesian analysis to literature observational data, aiming to relate the X -factor in galaxies to various observables. These authors found a similar relationship between X_{CO} and W_{CO} as in this paper. Their fit power-law index is ~ -0.31 .

6 SUMMARY

We have examined the effects of galactic environment on the CO–H₂ conversion factor in galaxies by coupling simulations of both quiescent disc and (merger-induced) starburst galaxy evolution at low and high redshift with dust and molecular line radiative transfer calculations. While quiescent disc galaxies at low- z with metallicities around solar tend to have mean X_{CO} values comparable to the Galactic mean, we find notable regimes in which X_{CO} may differ significantly from this value. In particular:

(i) *In low-metallicity galaxies*, photodissociation destroys CO more easily (due to a lack of dust), whereas the H₂ can self-shield more effectively. Hence, the amount of H₂ represented by CO emission rises, and the mean X_{CO} is greater than the Milky Way average.

(ii) *In regions of high surface density*, the gas temperature and velocity dispersion tend to be rather large. The former is due to heating of dust by young stars, and energy exchange with gas. The latter to the typical origins of high surface density galaxies: either major mergers or gravitationally unstable clumps in high- z gas-rich discs. In this regime, the velocity-integrated line intensity, W_{CO} , rises with respect to Σ_{H_2} , and there is a net decrease in the mean X_{CO} from the Galactic mean value.

(iii) *At high redshift*, gas-rich discs may have gravitationally unstable clumps that have moderate velocity dispersions, and high gas temperatures (owing to elevated SFRs compared to the Milky Way). These galaxies have X -factors ranging from the Galactic mean to a factor of a few lower. Our results for rapidly star-forming discs at $z \sim 2$ show that for a given set of physical conditions, gas-rich discs at high z have comparable X -factors to mergers at low z . Discs and mergers are not inherently different with respect to

their X -factors. Rather, current local conditions determine X_{CO} for a particular galaxy.

These results allow us to develop a fitting formula for X_{CO} in terms of gas metallicity and CO line intensity that varies smoothly (equation 10). Applying this formula to CO detections of galaxies at both low and high z , we find that all versions of the KS star formation relation ($\Sigma_{\text{SFR}} - \Sigma_{\text{mol}}$, $\Sigma_{\text{SFR}} - \Sigma_{\text{mol}}/t_{\text{dyn}}$ and $\Sigma_{\text{SFR}} - \Sigma_{\text{mol}}/t_{\text{ff}}$) may be described as unimodal with significantly reduced scatter compared to literature results that use bimodal X_{CO} values for discs and mergers.

The results from this work will enable relatively straightforward application of an X -factor which varies with galactic environment based simply on two observable parameters (metallicity and velocity-integrated CO line intensity).

ACKNOWLEDGMENTS

This work benefited from work done and conversations had at the Aspen Center for Physics. Emanuele Daddi, Robert Feldmann, Reinhard Genzel, Adam Leroy, Patrik Jonsson, Eric Murphy, Rahul Shetty and Andrew Skemer provided many helpful conversations and suggestions. We additionally thank Reinhard Genzel for providing us with digital copies of the relevant observational data from Tacconi et al. (2008) and Genzel et al. (2012), and Emanuele Daddi for providing us with the data from Daddi et al. (2010a). DN and LH acknowledge support from the NSF via grant AST-1009452. MK acknowledges support from: an Alfred P. Sloan Fellowship; the NSF through grants AST-0807739 and CAREER-0955300; and NASA through Astrophysics Theory and Fundamental Physics grant NNX09AK31G and a Chandra Theoretical Research Program grant. ECO acknowledges support from the NSF via grant AST-0908185. The simulations in this paper were run on the Odyssey cluster, supported by the Harvard Faculty of Arts and Sciences Research Computing Group.

REFERENCES

- Abdo A. A. et al., 2010a, *ApJ*, 709, L152
 Abdo A. A. et al., 2010b, *ApJ*, 710, 133
 Acciari V. A. et al., 2009, *Nature*, 462, 770
 Arimoto N., Sofue Y., Tsujimoto T., 1996, *PASJ*, 48, 275
 Barnes J. E., Hernquist L. E., 1991, *ApJ*, 370, L65
 Barnes J. E., Hernquist L., 1996, *ApJ*, 471, 115
 Bauer A., Springel V., 2011, preprint (arXiv:1109.4413)
 Bell T. A., Roueff E., Viti S., Williams D. A., 2006, *MNRAS*, 371, 1865
 Bell T. A., Viti S., Williams D. A., 2007, *MNRAS*, 378, 983
 Bernes C., 1979, *A&A*, 73, 67
 Bertsch D. L., Dame T. M., Fichtel C. E., Hunter S. D., Sreekumar P., Stacey J. G., Thaddeus P., 1993, *ApJ*, 416, 587
 Bigiel F., Leroy A., Walter F., Brinks E., de Blok W. J. G., Madore B., Thornley M. D., 2008, *AJ*, 136, 2846
 Blitz L., Rosolowsky E., 2006, *ApJ*, 650, 933
 Blitz L., Fukui Y., Kawamura A., Leroy A., Mizuno N., Rosolowsky E., 2007, in Reipurth B., Jewitt D., Keil K., eds, *Protostars and Planets V*. Univ. Arizona Press, Tucson, AZ, p. 81
 Bloemen J. B. G. M. et al., 1986, *A&A*, 154, 25
 Bolatto A. D., Leroy A. K., Rosolowsky E., Walter F., Blitz L., 2008, *ApJ*, 686, 948
 Bondi H., Hoyle F., 1944, *MNRAS*, 104, 273
 Boselli A., Lequeux J., Gavazzi G., 2002, *Ap&SS*, 281, 127
 Bothwell M. S. et al., 2010, *MNRAS*, 405, 219
 Bouché N. et al., 2007, *ApJ*, 671, 303
 Bournaud F. et al., 2008, *A&A*, 486, 741
 Bournaud F., Elmegreen B. G., Teyssier R., Block D. L., Puerari I., 2010, *MNRAS*, 409, 1088
 Bournaud F. et al., 2011, *ApJ*, 730, 4
 Bradford C. M., Nikola T., Stacey G. J., Bolatto A. D., Jackson J. M., Savage M. L., Davidson J. A., Higdon S. J., 2003, *ApJ*, 586, 891
 Bryant P. M., Scoville N. Z., 1999, *AJ*, 117, 2632
 Bullock J. S., Kolatt T. S., Sigad Y., Somerville R. S., Kravtsov A. V., Klypin A. A., Primack J. R., Dekel A., 2001, *MNRAS*, 321, 559
 Calura F., Pipino A., Matteucci F., 2008, *A&A*, 479, 669
 Carilli C. L. et al., 2010, *ApJ*, 714, 1407
 Ceverino D., Dekel A., Bournaud F., 2010, *MNRAS*, 404, 2151
 Cox T. J., Di Matteo T., Hernquist L., Hopkins P. F., Robertson B., Springel V., 2006a, *ApJ*, 643, 692
 Cox T. J. et al., 2006b, *ApJ*, 650, 791
 Cresci G., Mannucci F., Maiolino R., Marconi A., Gnerucci A., Magrini L., 2010, *Nature*, 467, 811
 Crosthwaite L. P., Turner J. L., 2007, *AJ*, 134, 1827
 Daddi E. et al., 2004, *ApJ*, 617, 746
 Daddi E. et al., 2005, *ApJ*, 631, L13
 Daddi E. et al., 2007, *ApJ*, 670, 156
 Daddi E. et al., 2010a, *ApJ*, 714, L118
 Daddi E. et al., 2010b, *ApJ*, 713, 686
 Dame T. M., Hartmann D., Thaddeus P., 2001, *ApJ*, 547, 792
 Davé R., Finlator K., Oppenheimer B. D., Fardal M., Katz N., Kereš D., Weinberg D. H., 2010, *MNRAS*, 404, 1355
 de Vries H. W., Thaddeus P., Heithausen A., 1987, *ApJ*, 319, 723
 Dekel A. et al., 2009, *Nature*, 457, 451
 Delahaye T., Fiasson A., Pohl M., Salati P., 2011, *A&A*, 531, A37
 Di Matteo T., Springel V., Hernquist L., 2005, *Nature*, 433, 604
 Dib S., Bell E., Burkert A., 2006, *ApJ*, 638, 797
 Dickman R. L., 1975, *ApJ*, 202, 50
 Donovan Meyer J. et al., 2012, *ApJ*, 744, 42
 Downes D., Solomon P. M., 1998, *ApJ*, 507, 615
 Downes D., Solomon P. M., 2003, *ApJ*, 582, 37
 Downes D., Solomon P. M., Radford S. J. E., 1993, *ApJ*, 414, L13
 Draine B. T., 2011, in Draine B. T., ed., *Physics of the Interstellar and Intergalactic Medium*
 Draine B. T., Li A., 2007, *ApJ*, 657, 810
 Dwek E., 1998, *ApJ*, 501, 643
 Elmegreen B. G., Bournaud F., Elmegreen D. M., 2008, *ApJ*, 688, 67
 Elmegreen B. G., Elmegreen D. M., Fernandez M. X., Lomonias J. J., 2009a, *ApJ*, 692, 12
 Elmegreen D. M., Elmegreen B. G., Marcus M. T., Shahinyan K., Yau A., Petersen M., 2009b, *ApJ*, 701, 306
 Engel H. et al., 2010, *ApJ*, 724, 233
 Erb D. K., Steidel C. C., Shapley A. E., Pettini M., Reddy N. A., Adelberger K. L., 2006, *ApJ*, 647, 128
 Evans N. J., II, et al., 2009, *ApJS*, 181, 321
 Feldmann R., Gnedin N. Y., Kravtsov A. V., 2011, preprint (arXiv:1112.1732)
 FörsterSchreiber N. M. et al., 2009, *ApJ*, 706, 1364
 Fukui Y., Kawamura A., 2010, *ARA&A*, 48, 547
 Genzel R. et al., 2010, *MNRAS*, 407, 2091
 Genzel R. et al., 2011, *ApJ*, 733, 101
 Genzel R. et al., 2012, *ApJ*, 746, 69
 Glover S. C. O., Mac Low M.-M., 2011, *MNRAS*, 412, 337
 Glover S. C. O., Federrath C., Mac Low M., Klessen R. S., 2010, *MNRAS*, 404, 2
 Goldsmith P. F., 2001, *ApJ*, 557, 736
 Greve T. R. et al., 2005, *MNRAS*, 359, 1165
 Groves B., Dopita M. A., Sutherland R. S., Kewley L. J., Fischera J., Leitherer C., Brandl B., van Breugel W., 2008, *ApJS*, 176, 438
 Guelin M., Zylka R., Mezger P. G., Haslam C. G. T., Kreysa E., Lemke R., Sievers A. W., 1993, *A&A*, 279, L37
 Hailey-Dunsheath S., Nikola T., Oberst T., Parshley S., Stacey G. J., Farrah D., Benford D. J., Staguhn J., 2008, in Kramer C., Aalto S., Simon R., eds, *EAS Publications Series*, Vol. 31, EDP Sciences, Les Ulis, p. 159

- Hayward C. C., Narayanan D., Jonsson P., Cox T. J., Kereš D., Hopkins P. F., Hernquist L., 2010, Treyer, M., Wyder, T. K., Neil J. D., Seibert M., Lee J. C., eds, ASP Conf. Ser. Vol. 440, UP2010: Have Observations Revealed a Variable Upper End of the Initial Mass Function? Astron. Soc. Pac., San Francisco, p. 369
- Hayward C. C., Kereš D., Jonsson P., Narayanan D., Cox T. J., Hernquist L., 2011, *ApJ*, 743, 159
- Hernquist L., 1989, *Nature*, 340, 687
- Hernquist L., 1990, *ApJ*, 356, 359
- Hinz J. L., Rieke G. H., 2006, *ApJ*, 646, 872
- Hollenbach D. J., Tielens A. G. G. M., 1999, *Rev. Modern Phys.*, 71, 173
- Hopkins P. F. et al., 2006a, *ApJS*, 163, 1
- Hopkins P. F. et al., 2006b, *ApJS*, 163, 50
- Hopkins P. F., Hernquist L., Cox T. J., Robertson B., Krause E., 2007a, *ApJ*, 669, 67
- Hopkins P. F., Richards G. T., Hernquist L., 2007b, *ApJ*, 654, 731
- Hopkins P. F., Cox T. J., Hernquist L., 2008a, *ApJ*, 689, 17
- Hopkins P. F. et al., 2008b, *ApJS*, 175, 356
- Hopkins P. F. et al., 2008c, *ApJS*, 175, 390
- Hopkins P. F. et al., 2008d, *ApJ*, 679, 156
- Hopkins P. F. et al., 2009, *MNRAS*, 397, 802
- Hopkins P. F., Younger J. D., Hayward C. C., Narayanan D., Hernquist L., 2010, *MNRAS*, 402, 1693
- Hunter S. D. et al., 1997, *ApJ*, 481, 205
- Israel F. P., 1997, *A&A*, 328, 471
- Jonsson P., 2006, *MNRAS*, 372, 2
- Jonsson P., Primack J. R., 2010, *New Astron.*, 15, 509
- Jonsson P., Cox T. J., Primack J. R., Somerville R. S., 2006, *ApJ*, 637, 255
- Jonsson P., Groves B. A., Cox T. J., 2010, *MNRAS*, 403, 17
- Joung M. R., Mac Low M., Bryan G. L., 2009, *ApJ*, 704, 137
- Juvela M., Ysard N., 2011, *ApJ*, 739, 63
- Kennicutt R. C., Jr, 1998a, *ARA&A*, 36, 189
- Kennicutt R. C., Jr, 1998b, *ApJ*, 498, 541
- Kennicutt R. C., Jr, et al., 2003, *PASP*, 115, 928
- Kennicutt R. C., Jr, et al., 2007, *ApJ*, 671, 333
- Keres D., Vogelsberger M., Sijacki D., Springel V., Hernquist L., 2011, preprint (arXiv:1109.4638)
- Krumholz M. R., Dekel A., 2010, *MNRAS*, 406, 112
- Krumholz M. R., Gnedin N. Y., 2011, *ApJ*, 729, 36
- Krumholz M. R., McKee C. F., 2005, *ApJ*, 630, 250
- Krumholz M. R., Tan J. C., 2007, *ApJ*, 654, 304
- Krumholz M. R., Thompson T. A., 2007, *ApJ*, 669, 289
- Krumholz M. R., McKee C. F., Tumlinson J., 2008, *ApJ*, 689, 865
- Krumholz M. R., McKee C. F., Tumlinson J., 2009a, *ApJ*, 693, 216
- Krumholz M. R., McKee C. F., Tumlinson J., 2009b, *ApJ*, 699, 850
- Krumholz M. R., Leroy A. K., McKee C. F., 2011, *ApJ*, 731, 25
- Krumholz M. R., Dekel A., McKee C. F., 2012, *ApJ*, 745, 69
- Kutner M. L., Leung C. M., 1985, *ApJ*, 291, 188
- Larson R. B., 1981, *MNRAS*, 194, 809
- Lee H., Bettens R. P. A., Herbst E., 1996, *A&AS*, 119, 111
- Leitherer C. et al., 1999, *ApJS*, 123, 3
- Lemaster M. N., Stone J. M., 2008, *ApJ*, 682, L97
- Leroy A., Bolatto A., Walter F., Blitz L., 2006, *ApJ*, 643, 825
- Leroy A. K. et al., 2011, *ApJ*, 737, 12
- Lombardi M., Alves J., Lada C. J., 2006, *A&A*, 454, 781
- McKee C. F., Krumholz M. R., 2010, *ApJ*, 709, 308
- McKee C. F., Ostriker J. P., 1977, *ApJ*, 218, 148
- Magdis G. E. et al., 2011, *ApJL*, 740, 15
- Maloney P., Black J. H., 1988, *ApJ*, 325, 389
- Markwardt C. B., 2009, in Bohlender D. A., Durand D., Dowler P., eds, ASP Conf. Ser. Vol. 411, *Astronomical Data Analysis Software and Systems XVIII*, Astron. Soc. Pac., San Francisco, p. 251
- Meier D. S., Turner J. L., Beck S. C., Gorjian V., Tsai C., Van Dyk S. D., 2010, *AJ*, 140, 1294
- Meijerink R., Spaans M., Israel F. P., 2007, *A&A*, 461, 793
- Mihos J. C., Hernquist L., 1994a, *ApJ*, 437, 611
- Mihos J. C., Hernquist L., 1994b, *ApJ*, 431, L9
- Mihos J. C., Hernquist L., 1996, *ApJ*, 464, 641
- Mo H. J., Mao S., White S. D. M., 1998, *MNRAS*, 295, 319
- Moster B. P., Macciò A. V., Somerville R. S., Naab T., Cox T. J., 2011a, *MNRAS*, 415, 3750
- Moster B. P., Macciò A. V., Somerville R. S., Naab T., Cox T. J., 2011b, preprint (arXiv/1108.1796)
- Narayanan D., Kulesa C. A., Boss A., Walker C. K., 2006, *ApJ*, 647, 1426
- Narayanan D., Cox T. J., Hayward C. C., Younger J. D., Hernquist L., 2009, *MNRAS*, 400, 1919
- Narayanan D., Hayward C. C., Cox T. J., Hernquist L., Jonsson P., Younger J. D., Groves B., 2010a, *MNRAS*, 401, 1613
- Narayanan D. et al., 2010b, *MNRAS*, 407, 1701
- Narayanan D., Cox T. J., Hayward C. C., Hernquist L., 2011a, *MNRAS*, 412, 287
- Narayanan D., Krumholz M., Ostriker E. C., Hernquist L., 2011b, *MNRAS*, 418, 664
- Obreschkow D., Rawlings S., 2009, *MNRAS*, 394, 1857
- Oka T., Hasegawa T., Hayashi M., Handa T., Sakamoto S., 1998, *ApJ*, 493, 730
- Ostriker E. C., Shetty R., 2011, *ApJ*, 731, 41
- Ostriker E. C., Stone J. M., Gammie C. F., 2001, *ApJ*, 546, 980
- Ostriker E. C., McKee C. F., Leroy A. K., 2010, *ApJ*, 721, 975
- Padoan P., Nordlund, Å., 2002, *ApJ*, 576, 870
- Papadopoulos P. P., Thi W.-F., Viti S., 2002, *ApJ*, 579, 270
- Papadopoulos P. P., Thi W.-F., Miniati F., Viti S., 2011, *MNRAS*, 414, 1705
- Pineda J. E., Caselli P., Goodman A. A., 2008, *ApJ*, 679, 481
- Price D. J., Federrath C., Brunt C. M., 2011, *ApJ*, 727, L21
- Robertson B., Yoshida N., Springel V., Hernquist L., 2004, *ApJ*, 606, 32
- Robertson B. et al., 2006, *ApJ*, 641, 21
- Robitaille T. P., Whitney B. A., 2010, *ApJ*, 710, L11
- Rosolowsky E., 2005, *PASP*, 117, 1403
- Rosolowsky E., 2007, *ApJ*, 654, 240
- Rosolowsky E., Engargiola G., Plambeck R., Blitz L., 2003, *ApJ*, 599, 258
- Sakamoto K. et al., 1999, *ApJ*, 514, 68
- Schaye J., Dalla Vecchia C., 2008, *MNRAS*, 383, 1210
- Schmidt M., 1959, *ApJ*, 129, 243
- Schuster K. F., Kramer C., Hirschfeld M., Garcia-Burillo S., Mookerjee B., 2007, *A&A*, 461, 143
- Scoville N. Z., Sargent A. I., Sanders D. B., Soifer B. T., 1991, *ApJ*, 366, L5
- Shapley A. E., 2011, *ARA&A*, 49, 525
- Shapley A. E., Erb D. K., Pettini M., Steidel C. C., Adelberger K. L., 2004, *ApJ*, 612, 108
- Shetty R. et al., 2011a, *MNRAS*, 412, 1686
- Shetty R. et al., 2011b, 415, 3253
- Sijacki D., Vogelsberger M., Keres D., Springel V., Hernquist L., 2011, preprint (arXiv:1109.3468)
- Snyder G. F., Cox T. J., Hayward C. C., Hernquist L., Jonsson P., 2011, *ApJ*, 741, 77
- Solomon P. M., Rivolo A. R., Barrett J., Yahil A., 1987, *ApJ*, 319, 730
- Solomon P. M., Downes D., Radford S. J. E., Barrett J. W., 1997, *ApJ*, 478, 144
- Springel V., 2000, *MNRAS*, 312, 859
- Springel V., 2005, *MNRAS*, 364, 1105
- Springel V., 2010, *MNRAS*, 401, 791
- Springel V., Hernquist L., 2003, *MNRAS*, 339, 289
- Springel V., Di Matteo T., Hernquist L., 2005, *MNRAS*, 361, 776
- Sternberg A., Dalgarno A., 1995, *ApJS*, 99, 565
- Strong A. W., Mattox J. R., 1996, *A&A*, 308, L21
- Tacconi L. J. et al., 2006, *ApJ*, 640, 228
- Tacconi L. J. et al., 2008, *ApJ*, 680, 246
- Tacconi L. J. et al., 2010, *Nature*, 463, 781
- Tan J. C., 2010, *ApJ*, 710, L88
- Torrey P., Cox T. J., Kewley L., Hernquist L., 2011, preprint (arXiv:1107.0001)
- Vázquez G. A., Leitherer C., 2005, *ApJ*, 621, 695
- Vladilo G., 1998, *ApJ*, 493, 583
- Vogelsberger M., Sijacki D., Keres D., Springel V., Hernquist L., 2011, preprint (arXiv:1109.1281)

- Wall W. F., 2007, MNRAS, 379, 674
 Watson D., 2011, A&A, 533, 16
 Weingartner J. C., Draine B. T., 2001, ApJ, 548, 296
 Wilson C. D., 1995, ApJ, 448, L97
 Wolfire M. G., Hollenbach D., McKee C. F., 2010, ApJ, 716, 1191
 Wong T., Blitz L., 2002, ApJ, 569, 157
 Younger J. D., Hayward C. C., Narayanan D., Cox T. J., Hernquist L.,
 Jonsson P., 2009, MNRAS, 396, L66

APPENDIX A: DETAILS OF NUMERICAL MODELLING

In this section, we detail the methodology governing our hydrodynamic modelling, calculations regarding the chemical and physical state of the ISM, and radiative transfer.

Table A1. Galaxy evolution simulation parameters. Column 1 refers to the model name. Column 2 is the baryonic mass in M_{\odot} . Column 3 is the merger mass ratio, with ‘N/A’ denoting when a galaxy is an isolated disc. Please note that we bin all mergers in the text as 1:1, 1:3 and 1:10, though these are approximate. Some 1:3-designated mergers may be in reality closer to 1:4, for example. Columns 4–7 refer to the orbit of a merger (with ‘N/A’ again referring to isolated discs). Column 8 is the initial baryonic gas fraction of the galaxy. Column 9 refers to the redshift of the simulation, and Column 10 is the final mass-weighted mean metallicity of the system in units of solar metallicity.

Model	M_{bar} (M_{\odot})	Mass ratio	θ_1	ϕ_1	θ_2	ϕ_2	f_g	z	Z'_f (Z_{\odot})
1	2	3	4	5	6	7	8	9	10
z3isob6	3.8×10^{11}	N/A	N/A	N/A	N/A	N/A	0.8	3	0.8
z3isob5	1.0×10^{11}	N/A	N/A	N/A	N/A	N/A	0.8	3	0.8
z3isob4	3.5×10^{10}	N/A	N/A	N/A	N/A	N/A	0.8	3	1.2
z3b6e	7.6×10^{11}	1:1	30	60	-30	45	0.8	3	0.9
z3b6b5e	4.8×10^{11}	1:3	30	60	-30	45	0.8	3	0.4
z3b5e	2.0×10^{11}	1:1	30	60	-30	45	0.8	3	0.9
z3b5b4e	1.4×10^{11}	1:3	30	60	-30	45	0.8	3	0.5
z3b5b3e	1.1×10^{11}	1:10	30	60	-30	45	0.8	3	0.8
z0isod5	4.5×10^{11}	N/A	N/A	N/A	N/A	N/A	0.4	0	1.7
z0isod4	1.6×10^{11}	N/A	N/A	N/A	N/A	N/A	0.4	0	0.8
z0isod3	5.6×10^{10}	N/A	N/A	N/A	N/A	N/A	0.4	0	0.9
z0d5e	8.9×10^{11}	1:1	30	60	-30	45	0.4	0	1.6
z0d5d4e	6.0×10^{11}	1:3	30	60	-30	45	0.4	0	0.8
z0d5d3e	5.0×10^{11}	1:10	30	60	-30	45	0.4	0	0.8
z0d4e	3.1×10^{11}	1:1	30	60	-30	45	0.4	0	1.4
z0d4h	3.1×10^{11}	1:1	0	0	0	0	0.4	0	1.2
z0d4i	3.1×10^{11}	1:1	0	0	71	30	0.4	0	1.1
z0d4j	3.1×10^{11}	1:1	-109	90	71	90	0.4	0	1
z0d4k	3.1×10^{11}	1:1	-109	30	71	-30	0.4	0	1.1
z0d4l	3.1×10^{11}	1:1	-109	30	180	0	0.4	0	1.2
z0d4n	3.1×10^{11}	1:1	-109	-30	71	30	0.4	0	1.2
z0d4o	3.1×10^{11}	1:1	-109	30	71	-30	0.4	0	1.1
z0d4p	3.1×10^{11}	1:1	-109	30	180	0	0.4	0	1.2
z0d4d3e	2.1×10^{11}	1:3	30	60	-30	45	0.4	0	0.8
z0d4d3i	2.1×10^{11}	1:3	0	0	71	30	0.4	0	1
z0d4d3j	2.1×10^{11}	1:3	-109	90	71	90	0.4	0	1.1
z0d4d3k	2.1×10^{11}	1:3	-109	30	71	-30	0.4	0	0.9
z0d4d3l	2.1×10^{11}	1:3	-109	30	180	0	0.4	0	1
z0d4d3m	2.1×10^{11}	1:3	0	0	71	90	0.4	0	1.1
z0d4d3n	2.1×10^{11}	1:3	-109	-30	71	30	0.4	0	0.9
z0d4d3o	2.1×10^{11}	1:3	-109	30	71	-30	0.4	0	1
z0d4d3p	2.1×10^{11}	1:3	-109	30	180	0	0.4	0	1
z0d4d2e	1.7×10^{11}	1:10	30	60	-30	45	0.4	0	0.8

A1 SPH galaxy evolution simulations

We run GADGET-3 SPH simulations for both model disc galaxies and galaxy mergers. The aim of these calculations is to return the spatial distribution and ages of stars, as well as the metal content and gas content as a function of location in the model galaxies.

GADGET-3 is a modified version of the publicly available GADGET-2 which employs algorithms for feedback from active galactic nuclei (AGN), and better load balancing on parallel processors. For a full description of the underlying algorithms of GADGET-2, see Springel (2005).

The ISM is modelled as multi-phase, with cold clouds embedded in a hotter phase (McKee & Ostriker 1977) which is practically implemented in the code via hybrid SPH particles (Springel & Hernquist 2003). The phases exchange mass via radiative cooling of the hotter phase, and supernova heating within the cold clouds. Within these cold clouds, stars form according to a volumetric Schmidt (1959) power-law relation with index 1.5 (Kennicutt 1998a). The normalization of this relation is set to match the surface-density $\Sigma_{\text{SFR}}-\Sigma_{\text{gas}}$ relation as observed in local galaxies by Kennicutt (1998a); (1998b). Experiments have found that imposing a volumetric Schmidt (1959) relation results in a power-law relation comparable to the observed one for the sorts of galaxies studied here (Mihos & Hernquist 1994a; Springel 2000; Cox et al. 2006b, though see Schaye & Dalla Vecchia 2008 for cases when this may not apply).⁹

The gas is initialized as primordial, with all metals forming as the simulation progresses. A mass fraction of stars (consistent with a Salpeter IMF) are assumed to die instantly in supernovae, and enrich the surrounding ISM with metals via an instantaneous recycling approximation using a yield of 0.02 (Springel & Hernquist 2003). Hence, gas has a non-zero metallicity from the first generation of star formation. We initialize in this manner in order to probe a large dynamic range of metallicities in the simulations for both disc galaxies and mergers. The typical final metallicities of each simulation examined are \sim solar, and we list these in the table.

Similarly, supernovae impact the surrounding ISM via energy deposition. This pressurization of the ISM is implemented via an ‘effective’ equation of state (EOS; Robertson et al. 2004; Springel et al. 2005). In the models presented here, we assume a relatively modest pressurization of the ISM ($q_{\text{EOS}} = 0.25$) for the model $z=0$ galaxies, and more extreme ($q_{\text{EOS}} = 1$) for the $z=2$ model galaxies. While the tests of Narayanan et al. (2011b) show that our results are insensitive to the choice of EOS within the Springel (2005) formalism, we are intentional with our choices. The large pressurization of the ISM for the high-redshift models is chosen to prevent runaway fragmentation in the dense, gas-rich environment (to be discussed shortly). Because our simulations are non-cosmological, and do not include gas accretion from the IGM (nor do they have algorithms for the inclusion of hot gas in the halo as in Moster et al. 2011a,b), extreme star formation in the early phases of a galaxy merger would deplete the gas supply prior to the galaxy merging. In this limit,

⁹ In Narayanan et al. (2011b), we explored the effects of modifying this SFR power-law index, and found our modelled X-factors were insensitive to variations in the SFR index so long as the index is >1 . Beyond this, in Narayanan et al. (2011b), we argued that a Schmidt index of unity is unlikely to describe the starburst environments modelled here as this choice of power-law index does not allow mergers to undergo a starburst. Similarly, observational (Bigiel et al. 2008) and theoretical work (Krumholz et al. 2009b; Ostriker & Shetty 2011) suggest that the SFR index may be superlinear in high-surface density environments.

galaxy mergers at high redshift would not undergo a starburst. Consequently, we employ a rather stiff EOS. We note that while this reduces the amount of fragmentation in the ISM (Springel 2005), large \sim kpc-scale clumps do still form and are dynamically unstable even in the model disc galaxies at $z \sim 2$, similar to both observations (e.g. Elmegreen, Bournaud & Elmegreen 2008; Elmegreen et al. 2009a,b; Genzel et al. 2011), and recent simulations with other codes (e.g. Bournaud et al. 2008, 2010, 2011; Dekel et al. 2009; Ceverino et al. 2010).

Black holes are included in the simulations as sink particles which accrete according to a Bondi–Lyttleton–Hoyle parametrization (Bondi & Hoyle 1944) with a fixed maximum rate corresponding to the Eddington limit. AGN feedback is included as thermal energy deposited by the central black hole. Specifically, 0.5 per cent of the accreted mass energy is reinjected spherically into the surrounding ISM which was chosen to allow merger remnants to match the present-day $M_{\text{BH}}-M_{\text{bulge}}$ relation (Di Matteo, Springel & Hernquist 2005; Springel et al. 2005; Hopkins et al. 2007a,b). As discussed in the appendix of Narayanan et al. (2011b), the inclusion of AGN feedback does not substantially impact the modelling of X_{CO} from galaxies in our simulations.

The discs are exponential, and initialized according to the Mo, Mao & White (1998) model, and embedded in a live cold dark matter halo with a Hernquist (1990) density distribution. The mergers simply involve discs constructed in this manner. The initial baryonic gas fractions are set to 40 per cent for the $z=0$ simulations, and 80 per cent for the high-redshift models. Because the galaxies consume their gas rapidly, the bulk of the high-redshift snapshots which are analysed in this study have gas fractions ranging from $f_{\text{g}} = 0.2-0.6$, comparable to recent CO measurements of $z \sim 1-2$ galaxies by Daddi et al. (2010b) and Tacconi et al. (2010).

The halo concentration and virial radius for a halo of a given mass are motivated by cosmological N -body simulations, and scaled to match the expected redshift-evolution following Bullock et al. (2001) and Robertson et al. (2006). The gravitational softening lengths are set at $100 h^{-1}$ pc for baryons and $200 h^{-1}$ pc for dark matter. We simulate a wide range of galaxy baryonic masses, merger mass ratios and merger orbits for both $z=0$ and $z=2$ galaxies.¹⁰ In the table, we summarize the physical parameters for the galaxy evolution models employed for this study, as well as the reasoning for the inclusion of that particular model.

We note that recently the reliability of SPH for cosmological modelling has been called into question by comparisons between simulations done with GADGET-3 and others done with the new moving mesh code AREPO developed by Springel (2010). In particular, Vogelsberger et al. (2011), Sijacki et al. (2011), Keres et al. (2011) and Bauer & Springel (2011) have shown that under certain conditions, broadly in circumstances where gas in very different phases is in close proximity or relative rapid motion, the results with the two codes can be very different. In our galaxy-scale simulations, however, we do not attempt to resolve the different phases of the ISM directly, and instead rely on subresolution models to describe the gas on small scales, a strategy dating back to early work by Hernquist (1989). For this reason, galaxy merger simulations done with AREPO yield results for the star formation history and mass fraction in newly formed stars that are virtually identical to those obtained with GADGET-3. Therefore, we believe that the results described here

are robust with respect to the numerical algorithm used to perform the hydrodynamics.

A2 Dust radiative transfer

We utilize the publicly available SUNRISE dust radiative transfer simulation package (Jonsson 2006; Jonsson et al. 2006, 2010; Jonsson & Primack 2010) for two purposes: to generate the adaptive mesh from the GADGET-3 simulations on which we run the radiative transfer, and to calculate dust temperatures in the ISM of the model galaxies.

In constructing the mesh, the physical conditions are projected on to a 5^3 base grid spanning 200 kpc. The cells recursively refine into 2^3 sub-cells based on the refinement criteria that the relative density variation of metals $\sigma_{\rho_{\text{m}}}/\langle \rho_{\text{m}} \rangle$ should be less than 0.1 and that the V -band optical depth across the cell is less than unity. The maximum refinement level is 11, so that the smallest cells on the grid are of the order of ~ 70 pc across.

For the dust radiative transfer, the sources of light are stellar clusters and the AGN. The stars emit a STARBURST99 spectrum (Leitherer et al. 1999; Vázquez & Leitherer 2005) with ages and metallicities known from the SPH simulations. The AGN emits a luminosity-dependent SED which is based on observations of unreddened type I quasars (Hopkins, Richards & Hernquist 2007b). The normalization of the input spectrum is set by the total luminosity of the black hole(s).

The radiation from stars and the AGN traverses the dusty ISM, and is scattered, absorbed and re-emitted. The evolving dust mass is set by assuming a constant dust to metals ratio comparable to that of the Galaxy (Dwek 1998; Vladilo 1998; Calura, Pipino & Matteucci 2008). We use the Weingartner & Draine (2001) dust grain model (with $R = 3.15$) as updated by Draine & Li (2007). The dust and radiation field are assumed to be in radiative equilibrium, and the dust temperatures are calculated iteratively.

The low-redshift and high-redshift models differ with regard to the specification of their ISM properties in the SUNRISE dust radiative transfer calculations. Following Narayanan et al. (2011b), for the low-redshift models, we assume that young (< 10 Myr) stellar clusters are embedded in PDRs and H II regions for some fraction of their lives. In this case, the STARBURST99 spectrum from the stellar clusters is replaced by SEDs derived from MAPPINGSIII photoionization models (Groves et al. 2008). The time-averaged covering fraction of PDRs is a free-parameter, and is set to be roughly 2–3 Myr. This value is motivated in part by simulations of Jonsson et al. (2010) who showed that this parameter choice when applied to models similar to ours produces synthetic SEDs comparable to those observed in the Spitzer Infrared Nearby Galaxy Survey sample (Kennicutt et al. 2003).

For very massive, gas-rich galaxies, during a merger the stellar densities can become so high that stellar clusters begin to overlap. At that point it makes more sense to describe the birthclouds that the clusters live in as surrounding the entire overlapping (super-)stellar cluster structures that form (sometimes as massive as many $\times 10^8 M_{\odot}$). The MAPPINGSIII photoionization models saturate for cluster masses of these sizes, and thus become inappropriate to use. Therefore, for the high-redshift calculations, we abandon the birthcloud model previously described, and assume the cold ISM is a uniform medium with a volume filling factor of unity. While in reality the ISM may be patchy on these scales, without any information as to what this patchiness may be like on resolution scales smaller than the SPH smoothing length, we are forced to make the simplest assumption possible. That said, this may be a reasonable choice.

¹⁰ The high-redshift galaxy simulations are actually initialized at $z=3$. This was chosen so that after the \sim Gyr typical for the galaxies to reach final coalescence when merging, the epoch would correspond roughly to $z \sim 2$.

Some evidence exists that in local mergers, a molecular ISM with a volume filling factor may blanket young stars for the majority of their lives (e.g. Downes & Solomon 1998; Sakamoto et al. 1999). In any case, the choice is made primarily due to simulation code constraints. In Narayanan et al. (2011b), we ran test cases examining the effects of both varying birthcloud clearing time-scales and the uniform volume filling fraction model, and found minimal effects on the derived X -factors.

A3 The thermal and chemical state of the molecular ISM

We assume the neutral mass in each cell in the adaptive mesh is locked into a spherical isothermal cloud at constant density. The surface density of the cloud is that which the simulation returns, though we impose a floor surface density of $100 M_{\odot} \text{pc}^{-2}$. This threshold surface density, comparable to the surface density of most molecular clouds in the Local Group (e.g. Solomon et al. 1987; Rosolowsky et al. 2003; Rosolowsky 2005, 2007; Blitz & Rosolowsky 2006; Blitz et al. 2007; Bolatto et al. 2008), is imposed to prevent clouds from having artificially low surface densities in large cells in the adaptive mesh. When clouds exceed this floor value, we consider them resolved.

We determine the H_2 – H I balance in these clouds utilizing the analytic model of Krumholz et al. (2008); (2009a) and McKee & Krumholz (2010) which treats the balance between photodissociation of H_2 molecules by Lyman–Werner band photons against the formation of molecules on grains. The equilibrium molecular fraction is given by

$$f_{\text{H}_2} \approx 1 - \frac{3}{4} \frac{s}{1 + 0.25s} \quad (\text{A1})$$

for $s < 2$ and $f_{\text{H}_2} = 0$ for $s \geq 2$. $s = \ln(1 + 0.6\chi + 0.01\chi^2)/(0.6\tau_c)$, where $\chi = 0.76(1 + 3.1Z'^{0.365})$, and $\tau_c = 0.066\Sigma_{\text{cloud}}/(M_{\odot}\text{pc}^{-2}) \times Z'$. Z' is the metallicity divided by the solar metallicity. A comparison of this method against fully time dependent chemical reaction networks by Krumholz & Gnedin (2011) finds good correspondence between the methods above metallicities of $Z' \approx 0.01$. While we explore the effects of metallicity on the X -factor in galaxies in these models, we never consider cases with metallicities lower than this value.

With the mass and surface density of the cloud known, the volumetric density is as well. We scale this density by a factor $e^{\sigma_p^2/2}$ to account for the turbulent compression of gas, where numerical simulations suggest that

$$\sigma_p^2 \approx \ln(1 + 3M_{\text{1D}}^2/4) \quad (\text{A2})$$

is a good approximation, where M_{1D} is the one-dimensional Mach number of the turbulence (Lemaster & Stone 2008; Ostriker, Stone & Gammie 2001; Padoan & Nordlund 2002; Price, Federrath & Brunt 2011). The Mach number is calculated by assuming the cloud temperature is 10 K (to avoid having to iterate as the temperature we will calculate is dependent on the density of the gas).

The velocity dispersion of the gas is determined as the mean square sum of the subgrid turbulent velocity dispersion and the resolved non-thermal velocity dispersion. The subgrid dispersion is calculated from the external pressure, $P = \rho_{\text{cell}}\sigma^2$, and has an imposed ceiling of 10 km s^{-1} , as suggested from galactic simulations which model turbulent energy driving and dissipation (Dib, Bell & Burkert 2006; Joung, Mac Low & Bryan 2009; Ostriker & Shetty 2011). The resolved non-thermal component is calculated from the standard deviation in the velocity dispersion in the nearest neighbour cells in the \hat{x} , \hat{y} and \hat{z} directions. In cases where the cloud is

unresolved, we simply assume the GMC is in virial balance, with virial parameter $\alpha_{\text{vir}} = 5\sigma_{\text{vir}}^2 R/(GM)$ of the order of unity so that

$$\sigma_{\text{vir}} = 2.2 \text{ kms}^{-1} \left[\frac{M}{10^5 M_{\odot}} \right]^{1/4} \quad (\text{A3})$$

where M is the mass of the cloud.

Finally, we calculate the temperature of the GMC based on the model developed by Krumholz et al. (2011). In this, we calculate the heating and cooling processes on the gas, the heating and cooling of the dust, and the energy exchange between the two. The heating processes of the gas are the grain photoelectric effect, and cosmic rays, and the cooling occurs via either CO or C II line emission. The dust is heated by the background radiation field, and cools thermally. Formally, if we denote heating processes by Γ , cooling by Λ , and energy exchange via Ψ , then we have

$$\Gamma_{\text{pe}} + \Gamma_{\text{CR}} - \Lambda_{\text{line}} + \Psi_{\text{gd}} = 0 \quad (\text{A4})$$

$$\Gamma_{\text{dust}} - \Lambda_{\text{dust}} - \Psi_{\text{gd}} = 0. \quad (\text{A5})$$

For brevity, we refer the reader to Krumholz et al. (2011) and Narayanan et al. (2011b) for the equations regarding the photoelectric effect and cosmic ray heating terms.

The gas cooling is assumed to happen either via C II or CO line emission. Following Wolfire et al. (2010), we approximate the fraction of hydrogen where CO is the dominant form of carbon by:

$$f_{\text{CO}} = f_{\text{H}_2} \times e^{-4(0.53 - 0.045 \ln \frac{G'_0}{n_{\text{H}}/\text{cm}^{-3}} - 0.097 \ln Z')/A_v} \quad (\text{A6})$$

which is consistent with the numerical work of Glover & Mac Low (2011). When f_{CO} is above 50 per cent, we assume the cooling happens via CO line cooling. Otherwise, C II is the dominant coolant. The extinction is converted via:

$$A_v = \frac{N_{\text{H}}}{1.87 \times 10^{21} \text{cm}^{-2}} Z' \quad (\text{A7})$$

(e.g. Watson 2011). We assume the dust is heated primarily by background infrared radiation as heating by UV radiation is likely to be highly suppressed by extinction. The IR radiation field is known from the SUNRISE dust radiative transfer modelling. The escape of the photons from the GMCs is calculated via the public escape probability code of Krumholz & Thompson (2007), which we describe in the subsequent section along with the other molecular line radiative transfer equations.

A4 Molecular line radiative transfer

Once we know the physical state of the GMCs in our model galaxies, we perform molecular line radiative transfer to calculate the CO intensity from the clouds. We first utilize an escape probability formalism to determine the escape fraction of photons from individual clouds, and then 3D non-LTE Monte Carlo molecular line radiative transfer calculations in order to calculate the transport of photons through the galaxies.

The escape probabilities are calculated using the publicly available code described in Krumholz & Thompson (2007). The levels are assumed to be in statistical equilibrium, and are calculated by balancing the excitation and deexcitation of CO by collisions with H_2 and He, absorption, stimulated emission and spontaneous emission via the rate equations:

$$\sum_l (C_{lu} + \beta_{lu} A_{lu}) f_l = \left[\sum_u (C_{ul} + \beta_{ul} A_{ul}) \right] f_u \quad (\text{A8})$$

$$\sum_i f_i = 1 \quad (\text{A9})$$

where C are the collisional rates, f the fractional level populations, A are the Einstein rate coefficients and β_{ul} is the escape probability for transition $u \rightarrow l$. The rate equations are re-arranged as an eigenvalue problem and solved with public packages available in the GNU Scientific Library.

β is well fitted by the approximate relation (Draine 2011)

$$\beta_{ul} \approx \frac{1}{1 + 0.5\tau_{ul}} \quad (\text{A10})$$

where the optical depth is

$$\tau_{ul} = \frac{g_u}{g_l} \frac{3A_{ul}\lambda_{ul}^3}{16(2\pi)^{3/2}\sigma} Q N_{\text{H}_2} f_l \left(1 - \frac{f_u g_l}{f_l g_u}\right) \quad (\text{A11})$$

where Q is the abundance of CO with respect to H_2 , g_l and g_u are the statistical weights of the levels, N_{H_2} is the column density of H_2 through the cloud, λ_{ul} is the wavelength of the transition and σ is the velocity dispersion in the cloud. We iterate equations (A8)–(A11) with standard Newton–Raphson methods until β and the populations are known for all levels simultaneously.

We then propagate the photons which escape the model GMCs through the galaxy following the methods of Bernes (1979).¹¹ The intrinsic line profile function is assumed to be Gaussian in nature with width given by the Doppler width. The model photons are emitted isotropically, and can be absorbed by GMCs they encounter along the path with a probability determined both by the volume filling factor of the GMC in the cell and the absorption line profile in the cell (thus accounting for decreasing effective optical depths owing to the absorption profile and emission profile shifting out of resonance when the line of sight velocity difference between the emitting and absorbing cell is large). When all the model photons have been emitted, the rate equations are again evaluated, level populations updated and new model photons are emitted. This process is iterated upon until convergence (a fractional difference in the level populations of 1×10^{-3}) is reached. In practice, this happens relatively quickly as velocity gradients in the galaxy render the ISM globally optically thin to most photons.

APPENDIX B: SIMULATED OBSERVATIONAL PROPERTIES OF MODEL GALAXIES

Because our methodology involves dust radiative transfer, we are able to make some comparisons to observed properties of galaxies. Here, we present a few comparisons to observations primarily to demonstrate that our simulated galaxies serve as reasonable analogues to the sorts of galaxies typically observed in large CO surveys.

At high redshift, the bulk of the galaxies observed in CO are identified according to two selection techniques: the BzK population and submillimetre-selected galaxies. BzK galaxies are defined by their optical colour ratios, and galaxies with blue $B - z$ colours, and red $z - K$ colours are typically denoted as star-forming BzK galaxies due to the presence of a Balmer break. In Fig. B1, we examine the optical colours of our model high- z discs. We redshift the discs to $z=2$, and plot the observed $(B - z)$ and $(z - K)$ colours

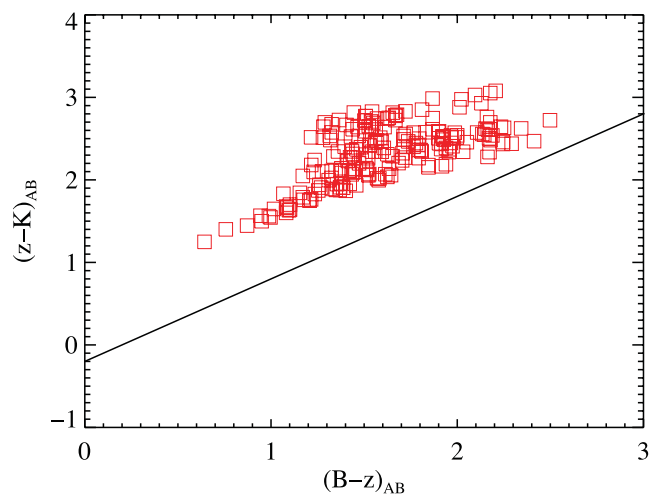


Figure B1. Synthetic $(B - z)$ and $(z - K)$ colours of model high- z disc galaxies. Each red square represents an individual snapshot from models z3isob6, z3isob5 and z3isob4. The model galaxies are redshifted to $z = 2$, and the colours are observed frame. Typically, galaxies above the solid line are observed to be star-forming discs (Daddi et al. 2004), and are representative of the sorts of ‘normal’ (not undergoing a burst of star formation) high- z galaxies observed in CO. Our model discs have optical observed-frame colours comparable to high- z discs.

as a comparison to $z \sim 2$ BzK galaxies. As originally discussed by Daddi et al. (2004), galaxies which fall above the line denoted in Fig. B1 tend to be disc-like in morphology (Daddi et al. 2005; Förster Schreiber et al. 2009). As is evident, our three model high- z discs all fall in the same space as observed BzK galaxies.

Narayanan et al. (2010a) and Hayward et al. (2011) presented a merger-driven model for the formation of high- z SMGs utilizing merger-models similar to our high-redshift mergers. These galaxies were seen to match the mean SEDs of observed SMGs, as well as the typical CO excitation patterns, line widths and morphologies (Narayanan et al. 2009). Furthermore, when convolving submillimetre-luminous duty cycles with theoretical galaxy merger rates and observed galaxy mass functions, Hayward et al. (2010) and Hayward et al. (in preparation) find that this merger-driven model provides a reasonable match to the observed number counts and redshift distribution of SMGs. In this sense, our model high- z mergers are likely reasonable analogues for the sorts of high- z starbursts observed in CO (e.g. Greve et al. 2005; Tacconi et al. 2006; Bouché et al. 2007; Tacconi et al. 2008; Bothwell et al. 2010; Genzel et al. 2010).

Our simulated mergers at low-redshift are similarly reasonable models for present-epoch ULIRGs. In Fig. B2, we show the evolution of the SFR, bolometric luminosity and $IRAS$ 25 $\mu\text{m}/60 \mu\text{m}$ flux density ratios for merger model z0d4e, the fiducial merger from Narayanan et al. (2011b). As is evident, when the galaxies merge (around $T \approx 0.85$ Gyr), the SFR undergoes a burst of comparable magnitude to the most heavily star-forming galaxies locally. Similarly, the bolometric luminosity rises to the point that the galaxy would be selectable as a ULIRG. The $IRAS$ infrared colours transition from ‘cool’ to ‘warm’ as the starburst and AGN heat the gas (Younger et al. 2009).

Beyond these few examples, a number of other comparisons to observations exist in the literature for this exact same set of simulations. For the high-redshift sample, the galaxies have been shown to reproduce observed properties of *Spitzer*-selected 24 μm sources (Narayanan et al. 2010b) and the properties of bright quasars

¹¹ In Narayanan et al. (2011b), we fully describe the equations employed for the galaxy-wide radiative transfer. The interested reader should refer to this paper for more detail, and here we summarize the relevant physical processes for the sake of brevity.

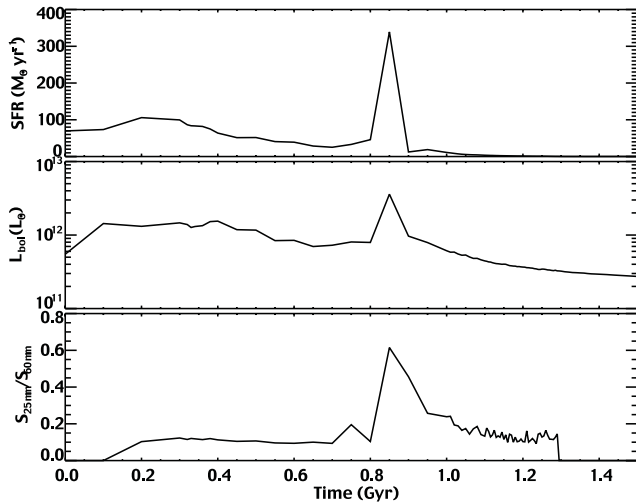


Figure B2. Evolution of SFR, L_{bol} and IRAS colour ratios for an example local merger (model z0d4e). Upon merging, the model galaxy undergoes a vigorous starburst, is selectable as a ULIRG and exhibits IRAS 25/60 μm ratios comparable to many local ULIRGs. Therefore, our simulated mergers are reasonable analogues for observed ULIRGs in the local Universe.

(Hopkins et al. 2006a,b). The low-redshift galaxy mergers have been shown to reproduce kinematic properties of early-type galaxies (Cox et al. 2006b), observed X-ray properties of metallicities in mergers (Cox et al. 2006a; Torrey et al. 2011), the broad-band colours of post-starburst galaxies (Snyder et al. 2011), and the structural properties of merging and elliptical galaxies (Hopkins et al. 2008c,d; Hopkins, Cox & Hernquist 2008a; Hopkins et al. 2009).

APPENDIX C: ENHANCED COSMIC RAY IONIZATION RATES IN STARBURSTS

In this section, we assess the validity of our assumption of a Galactic cosmic ray ionization rate. Cosmic rays may affect X_{CO} in galaxies by providing a source of heat for the molecular gas. Recalling the methodology presented in this Appendix, we assume a Galactic cosmic ray ionization rate in all model galaxies. It is conceivable that this assumption may break down in starbursts. Observations of

M82 by the VERITAS collaboration suggest a link between star formation and cosmic rays (Acciari et al. 2009). Similarly, detections of γ -rays from the Galaxy, Large Magellanic Cloud (LMC), NGC 253 and M82 by the *FERMI* group find a reasonable correlation between the γ -ray luminosity, and the product of the supernovae rate and gas mass (Abdo et al. 2010a). Since γ -rays are the product of cosmic rays with hydrogen atoms, a reasonable scaling may be that the cosmic ray ionization rate is linearly related to the SFR. Indeed, observations of local starbursts have suggested a potential for cosmic ray heated gas (e.g. Hailey-Dunsheath et al. 2008).

In order to test this, we have run a series of simulations in which we increase the cosmic ray ionization rate linearly with SFR. We assume a SFR of $2 M_{\odot} \text{ yr}^{-1}$ for the Milky Way (Robitaille & Whitney 2010). We span the range of physical conditions in our models, running a high- z 1:1 merger, high- z disc, low z 1:1 merger and low- z disc simulation.

In these examples, an increased cosmic ray ionization rate which scales linearly with the SFR does little to change X_{CO} . We look at a limiting case to illustrate why this is so. In merger-induced ULIRGs, where the SFR/cosmic ray flux can be a factor of as much as 200 higher than the Galactic value (e.g. SMGs), the minimum gas temperature imposed by cosmic ray-heating is $\sim 30\text{--}50$ K, depending on the density of the gas (Papadopoulos et al. 2011). In these environments, the dust temperature is typically not very different from this. For example, in Narayanan et al. (2011b), we found the mass-weighted mean dust temperature of a local merger was ~ 70 K. In short, the scenarios in which the cosmic ray ionization rate may be increased have a large gas temperature anyway due to high dust temperatures and efficient energy exchange between the two at high densities. We therefore tentatively conclude that enhanced cosmic ray ionization rates do not affect X_{CO} in starburst environments, though we caution that if the cosmic ray heating rate rises much faster than linearly with SFR (see e.g. Bradford et al. 2003), then this inference may break down. Based on the calculations of Papadopoulos et al. (2011), we estimate that the cosmic ray heating would affect our results significantly only if the ratios of the cosmic ray heating rates in mergers and isolated galaxies were at least 10 times greater than their ratios of SFR.

This paper has been typeset from a $\text{\TeX}/\text{\LaTeX}$ file prepared by the author.